

# University of St Andrews



Full metadata for this thesis is available in  
St Andrews Research Repository  
at:

<http://research-repository.st-andrews.ac.uk/>

This thesis is protected by original copyright



# **BORON SUBSTITUTION IN CERAMIC AND MICROPOROUS MATERIALS**

A thesis presented for the degree of

*Master of Philosophy*

in the Faculty of Science of the University of St Andrews

by Martin J. Maple, BSc (Hons), GRSC

March 2000



School of Chemistry

St Andrews



Th D 604

# Declarations

I, Martin J. Maple, hereby certify that this thesis, which is approximately 13 000 words in length, has been written by me, that it is the record of work carried out by me and that it has not been submitted in any previous application for a higher degree.

Signature of candidate

31 March 2000

I was admitted as a research student and candidate for the degree of Master of Philosophy in September 1998; the higher study for which this is a record was carried out in the University of St Andrews between 1998 and 1999.

Signature of candidate

31 March 2000

I hereby certify that the candidate has fulfilled the conditions of the Resolution and Regulations appropriate for the degree of Master of Philosophy in the University of St Andrews and that the candidate is qualified to submit this thesis in application for that degree.

Signature of supervisor

31 March 2000

In submitting this thesis to the University of St Andrews I understand that I am giving permission for it to be made available for use in accordance with the regulations of the University Library for the time being in force, subject to any copyright vested in the work not being affected thereby. I also understand that the title and abstract will be published, and that a copy of the work may be made available and supplied to any *bona fide* library or research worker.

Signature of candidate

31 March 2000

# Abstract

The effect of boron on the crystallisation and properties of two classes of useful crystalline material, namely ceramics and microporous solids, has been considered.

The ceramic chosen was mullite and materials of varying composition within the  $\text{Al}_2\text{O}_3\text{-SiO}_2\text{-B}_2\text{O}_3$  phase diagram were prepared via sol-gel synthesis and treatment at elevated temperatures (900 – 1200 °C). Resultant products were characterised by powder X-ray diffraction and MAS NMR spectroscopy. Boron was found to accelerate crystallisation of aluminosilicate mullites but may be partially lost at higher temperatures. Aluminoborate mullite was observed which broke down at higher temperatures to the known phase  $9\text{Al}_2\text{O}_3\cdot 2\text{B}_2\text{O}_3$  and alumina. Boro-mullite that was phase pure by X-ray diffraction and MAS NMR was seen to crystallise over a wider range of compositions than previously reported.  $^{11}\text{B}$  MAS NMR confirms that the boron exists in trigonal co-ordination. Assuming the boron is present in the mullite structure, it is hypothesised to be in a related trigonal site to that observed in  $9\text{Al}_2\text{O}_3\cdot 2\text{B}_2\text{O}_3$ , rather than in a tetrahedral site as previously proposed.

The aluminophosphate family of microporous materials was investigated and hydrothermal experiments performed to screen two families of primary amines as templates (1: isopropylamine, N-isopropylethylenediamine and N'-isopropyl-diethylenetriamine, 2: *trans*-1,4-diaminocyclohexane, *trans*-1,2-diaminocyclohexane and *cis*-1,2-diaminocyclohexane). Selected materials were investigated further by single crystal or synchrotron powder diffraction and MAS NMR. Analysis was performed to determine the quantity of boron substituting into the aluminophosphate framework but this was found to be very small. As a further investigation in the utility of systematic experimental design in hydrothermal synthesis, a literature synthesis of a microporous aluminoborate was investigated and conditions varied to give a pure phase.

# Acknowledgements

I would first like to thank Paul Wright, my supervisor, for his knowledge and enthusiasm during this project, and his patience with me during the writing of this thesis.

I would also like to acknowledge the assistance of others: Dr Philip Lightfoot (St Andrews) for his expertise in X-ray diffraction, Dr David Appleby (EPSRC Solid State NMR Service, Durham) and Melanja Smith (St Andrews) for the MAS NMR, Dr Mark Roberts (SRS, CLRC Daresbury Laboratory) for guidance at the synchrotron.

I should also like to thank the members of the Wright and Lightfoot groups and especially Zoe Lethbridge and David Woodcock, for their help, support and humour during this project.

And finally, to Borax Europe Ltd, for funding.

# Contents

<b>Chapter 1. Introduction</b>	<b>1</b>
1.1. Boron	1
1.2. Ceramics	2
1.3. Microporous Solids	3
1.4. Experimental Design	4
1.5. References	5
<b>Chapter 2. Analytical Techniques</b>	<b>7</b>
2.1. X-ray Diffraction	7
2.1.1. Obtaining Diffraction Data	9
2.1.2. The Rietveld Method	9
2.1.3. Quantitative X-ray Methods	11
2.2. Nuclear Magnetic Resonance Spectroscopy	12
2.2.1. NMR in the Solid State	16
2.2.1.1. Sources of Line Broadening	16
2.2.1.2. Overcoming Line Broadening: Magic Angle Spinning (MAS)	16
2.2.1.3. Spin > 1/2 Nuclei	17
2.3. Statistical Experimental Design	18
2.3.1. Response Surface Designs	18
2.3.2. Experimental Structure	19
2.4. References	20
<b>Chapter 3. Boron Substitution in Microporous Materials</b>	<b>22</b>
3.1. Abstract	22
3.2. Introduction	22
3.2.1. Zeolites	23
3.2.2. Zeotypes	24
3.3. Experimental	26
3.3.1. Boro-aluminophosphate Synthesis	26
3.3.1.1. Diaminocyclohexane	26
3.3.1.2. Isopropylamine and Derivatives	28
3.3.2. Aluminoborate Synthesis	28
3.3.3. Crystallography	29
3.3.4. MAS NMR Spectroscopy	30
3.3.5. Atomic Adsorption Spectroscopy	30

3.4. Results	30
3.4.1. Boro-aluminophosphate Materials	30
3.4.1.1. Diaminocyclohexane	30
3.4.1.2. Isopropylamine and Derivatives	33
3.4.2. Aluminoborate Materials	35
3.5. Discussion	39
3.5.1 Boro-aluminophosphate Materials	39
3.5.2. Aluminoborate Materials	39
3.6. Conclusion and Further Work	40
3.7. References	40

## **Chapter 4. Boron Substituted Mullite Ceramics** **42**

4.1. Abstract	42
4.2. Introduction	42
4.2.1. The Structure of Sillimanite	42
4.2.2. Aluminosilicate Mullite	44
4.2.3. Boron Substitution in Mullite	47
4.3. Experimental	50
4.3.1. Synthesis	50
4.3.2. Crystallography	51
4.3.3. MAS NMR Spectroscopy	52
4.4 Results	52
4.4.1. Aluminoborate Phases	54
4.4.1.1. XRD Results	54
4.4.1.2. NMR Results	58
4.4.2. Boro-aluminosilicate Phases	60
4.4.2.1. XRD Results	60
4.4.2.2. Rietveld Refinements	65
4.4.2.3. NMR Results	66
4.5. Discussion	72
4.6. Conclusions	72
4.7. Further Work	73
4.8. References	73

# Chapter One

## Introduction

One of the most engaging things about crystalline solids is the certainty that arrives with a full understanding of the structure. Such materials find applications in diverse areas, and are of interest for this reason, but very often it is a knowledge of the structure that reveals the root of the materials' bulk properties. Examples range from heterogeneous catalysts to superconductors.<sup>1</sup>

The aims of this project were twofold. Firstly, to investigate the role of boron in the crystallisation of useful materials, and secondly, to examine the boron-containing materials' properties.

Two classes of crystalline material were chosen for study: ceramics and microporous solids. Specifically, in the former class: boro-mullite and in the latter: boro-aluminophosphate and aluminoborate. Additionally, a comparison was made between the conventional triangular composition diagram approach and the statistical experimental design technique for examining the factors affecting the nature of the product. These methods find most effective application with the two different types of material that were studied. Composition diagrams lend themselves to ceramic systems where the number of factors is small while statistical techniques are useful in optimising many parameters found in hydrothermal preparations.

### 1.1. Boron

Small size and high ionisation potentials (the first at 8.296 eV) characterise boron which more strongly resembles silicon, than aluminium, in its properties and reactions; this may be illustrated by comparing  $B(OH)_3$  and  $Al(OH)_3$ , the former being weakly acidic in contrast to the latter which is mainly basic, but with some amphoteric character. Boric acid acts not as a proton donor but a Lewis acid, accepting  $OH^-$  and releasing a proton from water.

Boron compounds of oxygen are particularly important as the B–O bond is very strong (560 kJ in  $\text{BO}_3$ , 790 kJ in  $\text{BO}_4$ ). Many can be synthesised from boric acid which has a large negative heat of solution, thus its solubility increases markedly with temperature. The species formed also depend on  $\text{pH}$ , moving from simple to polymeric ions:



to more complex species:  $\text{B}_5\text{O}_6(\text{OH})_4^-$ ,  $\text{B}_3\text{O}_3(\text{OH})_4^-$  and  $\text{B}_4\text{O}_5(\text{OH})_4^{2-}$ , as the  $\text{pH}$  increases, until attack on the neutral trigonal boron is favoured and  $\text{B}(\text{OH})_4^-$  is formed.<sup>2</sup>

Boron is used industrially in ceramics, glasses, medicine, fuel technology, nuclear waste storage and many others.<sup>3</sup> It occurs widely (naturally in 208 compounds) in arid parts of California, and elsewhere, as borax ( $\text{Na}_2\text{B}_4\text{O}_5(\text{OH})_4 \cdot 8\text{H}_2\text{O}$ ) and kernite ( $\text{Na}_2\text{B}_4\text{O}_5(\text{OH})_4 \cdot 2\text{H}_2\text{O}$ ).<sup>4</sup> Oxygen bearing mineral forms are divided into two: borates and borosilicates. In the former, boron polyhedra are isolated or share vertices, while in the latter they share vertices chiefly with either boron or silicon tetrahedra. The boron may be in planar triangular or tetrahedral co-ordination with oxygen or hydroxyl groups; pressure at synthesis influences which species predominate:  $\text{BO}_3$  at low pressure and  $\text{BO}_4$  when it is higher.<sup>5</sup> An example where boron co-ordinates trigonally is jeremejevite ( $6\text{Al}_2\text{O}_3 \cdot 5\text{B}_2\text{O}_3 \cdot 3\text{H}_2\text{O}$ ), while in the zeolites and boron analogues of the aluminosilicate feldspars, such as reedmergnerite ( $\text{NaBSi}_3\text{O}_8$ ), boron can be seen in tetrahedral co-ordination. As a consequence of this ability to exist in two co-ordination environments, boron containing compounds exhibit a rich structural chemistry.

## 1.2. Ceramics

Aluminosilicate mullite is an increasingly important ceramic material, not only because of its excellent thermal stability and creep resistance, but also for its low thermal expansion and thermal conductivity coefficients.<sup>6</sup> Recently a novel honeycomb composite structure of macroporous mullite and microporous ZSM-5 (structure type: MFI), crystallised *in situ*, has been fabricated.<sup>7</sup> Applications of such

materials may include membranes, cation exchange separations and as automotive or other catalysts. Currently a cordierite ceramic honeycomb is used in auto-catalysts but the introduction of a microporous solid would have many advantages.

The role of boron in the crystallisation of other aluminosilicate ceramics has been studied in this and other laboratories. For example, boron substitutes in small amounts into the tetrahedral sites of both cordierite ( $\text{Mg}_2\text{Al}_4\text{Si}_5\text{O}_{18}$ ) and  $\beta$ -eucryptite ( $\text{LiAlSiO}_4$ ).<sup>8</sup> Leucite<sup>9</sup> ( $\text{KAl}_{(1-x)}\text{B}_x\text{Si}_2\text{O}_6$ ) has been prepared by a sol-gel route at 900 – 1250°C, with boron content between zero and one. Infra-red spectroscopy revealed tetrahedral  $\text{BO}_4$  units but no three co-ordinate boron. Preliminary evidence for the synthesis of boro-mullites has been presented by Werding and Schreyer in the form of a phase diagram.<sup>10</sup> Among other metal borates, comparisons have been made between the structures of painite ( $\text{CaZrB}[\text{Al}_9\text{O}_{18}]$ ), fluorborite ( $\text{B}_3[\text{Mg}_9(\text{F},\text{OH})_9\text{O}_9]$ ) and jeremejevite ( $\text{B}_5[\diamond_3\text{Al}_6(\text{OH})_3\text{O}_{15}]$   $\diamond$  = vacancy), which already contain boron.<sup>11</sup> Each structure may be thought of as an octahedral framework (shown here in square-brackets) with boron in triangular co-ordination.

Crystallographically the solution of the incommensurate structure of mullite is non-trivial and has been the subject of ongoing studies.<sup>12</sup> Boro-aluminosilicate and aluminoborate mullites have been reported but the composition and structural properties are not well understood. The addition of boron has been suggested to result in the substitution  $\text{B}^{3+}(\text{tetr}) \leftrightarrow \text{Al}^{3+}(\text{tetr})$ .<sup>13</sup>

In this thesis the  $\text{Al}_2\text{O}_3$ - $\text{SiO}_2$ - $\text{B}_2\text{O}_3$  phase diagram has been reinvestigated; boro-aluminosilicate and aluminoborate mullite and a related phase of composition  $9\text{Al}_2\text{O}_3 \cdot 2\text{B}_2\text{O}_3$ , have been studied.

### 1.3. Microporous Solids

Microporous solids form another group of industrially significant materials. They may be divided into two broad classes: zeolites and zeotypes, the former being strictly aluminosilicates and the latter representing all other materials.<sup>14</sup> Microporous solids have found wide application as heterogeneous catalysts and in ion-exchange and sorption technologies. Extensive reviews are to be found elsewhere.<sup>15</sup>

Boron has been found to substitute for aluminium in zeolites (the so-called boralites), giving solids of mild Brønsted acid strength. Titanium boralites of structure type MFI, have been reported with varying amounts of boron incorporated as  $\text{BO}_4$  tetrahedra within the framework.<sup>16</sup> The boron is partially removed from its tetrahedral site on calcination but this could be reduced by decreasing the amount of titanium in the solid. Boron may also be included in the aluminosilicate analogue of this material: ZSM-5 which can contain both three and four co-ordinate species.<sup>17</sup>

A rare example of complete boron substitution for both silicon and aluminium in a zeolite is seen in the zincoborate  $\text{Zn}_4\text{O}(\text{BO}_2)_6$ , analogous in structure to sodalite (structure type: SOD).<sup>18</sup> The hilgardite group of minerals— $\text{Ca}_2[\text{B}_5\text{O}_9]\text{Cl}\cdot\text{H}_2\text{O}$ , have structures containing the pentaborate polyanion  $[\text{B}_5\text{O}_{12}]^{9-}$  which comprises three borate tetrahedra and two borate triangles.<sup>19</sup> They are microporous zeotypes that have piezoelectric properties. Borophosphate materials have also been reported, the first open-framework material being  $\text{CoB}_2\text{P}_3\text{O}_{12}(\text{OH})\cdot\text{C}_2\text{H}_{10}\text{N}_2$  (which contains boron tetrahedra).<sup>20</sup> There is little literature evidence for the existence of boro-aluminophosphates.<sup>21</sup>

The hydrothermal synthesis of boro-aluminophosphate materials and an aluminoborate phase have been investigated and their conditions of synthesis examined with statistically designed experiments. Combinations of factors, such as temperature and time, may be studied with optimum efficiency in a very few experiments by this method.

## 1.4. Experimental Design

In ceramic systems the approach is typically to develop the phase diagram.<sup>22</sup> Temperature and time are usually the critical factors in determining products at any given composition, so that even with a ternary system, such as  $\text{Al}_2\text{O}_3\text{--SiO}_2\text{--B}_2\text{O}_3$ , the system is easy to explore.

In contrast, the investigation and optimisation of parameters that control the product of a hydrothermal preparation is non-trivial. The large number of variables (temperature, time, heating programme, concentration, solvent, agitation, ageing etc.) does not facilitate systematic research with phase diagrams because of the

complexity of the system. Yet it is often crucially important that a synthesis be optimised in a particular way, be it to obtain large single crystals (to facilitate structure solution of novel materials) or fine powders (for efficient catalysts). Purity is also critical as separation of phases is difficult. These criteria are, however, extremely difficult to meet because of the nature of hydrothermal synthesis. Insufficient understanding of the crystallisation process, due to complex gel chemistry, and the interactions of reaction variables mean that optimum synthesis conditions are unique to each new material. For this reason an efficient method for examining the factors that yield the required response is required: sampling techniques can be usefully employed to reduce the number of experiments necessary to obtain these data.<sup>23</sup> The theory behind such an approach is described in the second chapter.

## 1.5. References

1. C. N. R. Rao and J. Gopalakrishnan, *New Directions in Solid State Chemistry*, Cambridge University Press, Cambridge, 2nd edn., 1997.
2. F. A. Cotton and G. Wilkinson, *Advanced Inorganic Chemistry*, John Wiley and Sons, New York, 5th edn., 1988, ch. 6, pp. 168–170.
3. C. R. Hammond, in *CRC Handbook of Chemistry and Physics*, ed. D. R. Lide, CRC Press, Boca Raton, 80th edn., 1999, ch. 4, pp. 5–6.
4. L. M. Anovitz and E. S. Grew, in *Reviews in Mineralogy*, eds. P. H. Ribbe, Mineralogical Society of America, Washington DC, 1st edn., 1996, vol. 33, ch. 1, p. 2.
5. G. Werding and W. Schreyer, in *Reviews in Mineralogy*, ed. P. H. Ribbe, Mineralogical Society of America, Washington DC, 1st edn., 1996, vol. 33, ch. 3, p. 117.
6. H. Schneider, K. Rodewald and E. Eberhard, *J. Am. Ceram. Soc.*, 1993, **76**, 2896.
7. S. Komarneni, H. Katsuki and S. Furuta, *J. Mater. Chem.*, 1998, **8**, 2327.
8. P. A. Wright and M. Sasidharan, unpublished work.
9. D. Mazza, M. L. Borlera, C. Brisi and B. Onida, *J. Eur. Ceram. Soc.*, 1997, **17**, 951.

10. G. Werding and W. Schreyer, in *Reviews in Mineralogy*, ed. P. H. Ribbe, Mineralogical Society of America, Washington DC, 1st edn., 1996, vol. 33, ch. 3, p. 127.
11. P. B. Moore and T. Araki, *Am. Mineral.*, 1976, **61**, 88.
12. P. Rehak, G. Kunath-Fandrel, P. Losso, B. Hildmann, H. Schneider and C. Jäger, *Am. Mineral.*, 1998, **83**, 1266.
13. D. Mazza and M. Vallino, *J. Am. Ceram. Soc.*, 1992, **75**, 1929.
14. J. M. Newsam, in *Solid State Chemistry Compounds*, eds, A. K. Cheetham and P. Day, Oxford University Press, Oxford, 1st edn., 1996, ch. 7, pp. 234–280.
15. J. M. Thomas, *Faraday Discuss.*, 1996, **105**, 1; I. W. C. W. Arends, R. A. Sheldon, M. Wallau and U. Schuchardt, *Angew. Chem. Int. Ed. Engl.*, 1997, **36**, 1144.
16. D. T. On, M. P. Kapoor, L. Bonneviot, S. Kaliaguine and Z. Gabelica, *J. Chem. Soc., Faraday Trans.*, 1996, **92**, 1031.
17. C. Fild, H. Eckert and H. Koller, *Angew. Chem. Int. Ed.*, 1998, **37**, 2505.
18. W. T. A. Harrison, T. E. Gier and G. D. Stucky, *Angew. Chem. Int. Ed. Engl.*, 1993, **32**, 724.
19. S. Ghose and C. Wan, *Nature (London)*, 1977, **270**, 594; S. Ghose, *Am. Mineral.*, 1982, **67**, 1265.
20. S. C. Sevov, *Angew. Chem. Int. Ed. Engl.*, 1996, **35**, 2630.
21. I. P. Appleyard, R. K. Harris and F. R. Fitch, *Zeolites*, 1986, **6**, 428.
22. A. R. West, *Solid State Chemistry and its Application*, John Wiley and Sons, New York, 1st edn. 1984, ch. 11, pp. 374–416.
23. W. P. Gardiner, *Statistical Analysis Methods for Chemists*, Royal Society of Chemistry, Cambridge, 1st edn., 1997.

## Chapter Two

# Analytical Techniques

With modern diffraction and spectroscopic techniques the structure and composition of solid materials can be probed with ever more precision. X-ray diffraction (XRD) and magic angle spinning nuclear magnetic resonance (MAS NMR) spectroscopy have proved to be the most powerful means for investigating the crystalline systems reported here.

### 2.1. X-ray Diffraction

The phenomenon of diffraction is the interference caused by a periodic object, in the path of a wave, when the dimensions of the diffracting object are comparable to the wavelength of the radiation. The motif of varying intensities that results is called the diffraction pattern.

In 1912 von Laue proposed that X-rays were composed of such short wavelength radiation that successive layers in a crystal might form an effective diffraction grating.<sup>1</sup> This was demonstrated the same year by Friedrich and Knipping, who directed a beam of X-rays at a large crystal of copper sulfate. W. H. and W. L. Bragg refined the experimental technique studying sodium chloride, utilising monochromatic radiation in place of the 'white' radiation used in the original work. At the same time they developed a spectrometer which measured the intensity of the diffracted X-ray beam by monitoring the amount of ionisation which it could produce.

When a beam of X-rays is incident upon a crystal, some of the radiation will pass straight through, while a fraction will be diffracted by the planes of atoms within the structure. W. L. Bragg noted that X-rays are diffracted only at specific orientations of the crystal, with respect to the source and detector (Figure 2.1.).

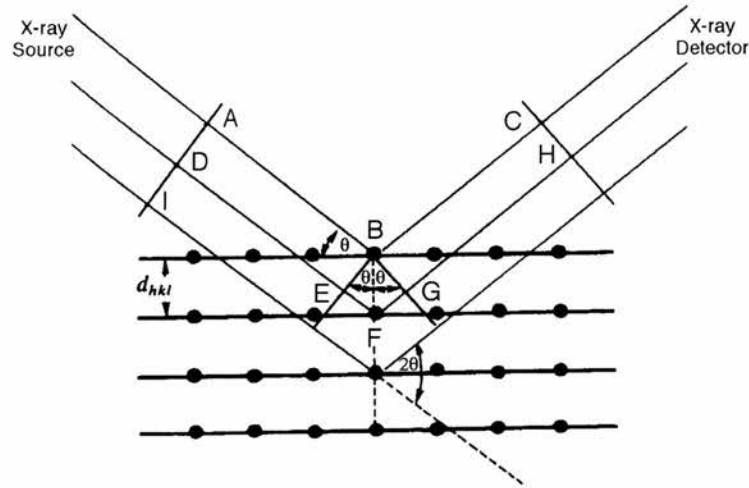


**Figure 2.1.** X-rays diffracted from the Miller planes of a crystal may only be detected if they satisfy the Bragg equation and constructively interfere.

The lines joining the points in the diagram mark a set of lattice planes with Miller indices  $hkl$  and an interplanar spacing  $d_{hkl}$ . A parallel beam of X-rays is incident onto the planes at an angle  $\theta_{hkl}$ . The frequency, wavelength and angle of the diffracted beam are identical to those of the incident beam.

The beam of X-radiation penetrates the crystal such that atoms in successive rows scatter the X-rays in all directions. All the X-rays scattered by the atoms are in phase only if the angle of incidence  $\theta$  to the lattice planes, satisfies certain conditions, derived first by Laue.<sup>2</sup> This is best considered in terms of the Bragg 'reflection' analogy. For the 'reflected' beams to emerge as a single beam of reasonable intensity they must reinforce (constructively interfere). The path lengths of the interfering beams must differ by an integral number of wavelengths for this to occur. From Figure 2.1. it can be seen that the difference in path length between the two beams is:

$$(DF + FH) - (AB + BC) \quad \text{Eqn. 2.1.}$$

but since  $AB = DE$  and  $BC = GH$  the difference in path length becomes  $EF + FG$ . Now  $EF = FG = d_{hkl} \sin \theta_{hkl}$  which implies the difference in path length is  $2d_{hkl} \sin \theta_{hkl}$ . This must be equal to an integral number of wavelengths  $n$ . If the wavelength of the X-radiation is  $\lambda$ , then:

$$n\lambda = 2d_{hkl} \sin \theta_{hkl} \quad \text{Eqn. 2.2.}$$

This is the Bragg equation, the condition for reinforcement to occur for X-rays reflected from parallel rows of lattice points in a crystal.

### 2.1.1. Obtaining Diffraction Data<sup>3</sup>

The structure of suitably large crystals can be obtained easily with laboratory based single crystal diffractometers. In this instance the crystal is mounted on a filament with glue and placed in the four-circle diffractometer. This consists of an X-ray source, and X-ray detector, a goniometer that orients the crystal and a computer to control the experiment and process the results.

However, a finely ground crystalline powder contains a large number of crystallites, that are oriented randomly with respect to each other. If such a sample is placed in the path of a monochromatic X-ray beam, diffraction will occur from the planes in those crystallites that happen to be oriented at the correct angle to fulfil the Bragg condition. Powder diffraction patterns can be collected in step scan mode where intensity is measured for a given period of time before the detector is stepped to the next position around the  $2\theta$ -axis. Solid samples may be identified by comparing the position of the diffraction lines, and their intensities, with a large database.<sup>4</sup>

The difficulty with the powder method for structure solution lies in indexing the pattern, that is, deciding which Miller planes are responsible for each reflection. Accurate unit cell dimensions can be calculated with this information and analysis carried out to examine possible systematic absences to suggest a space group. The Rietveld method can then be used to refine a structural model.

### 2.1.2. The Rietveld Method<sup>5</sup>

With the Rietveld method a least squares refinement is carried out until the best-fit between the whole powder diffraction profile and the entire calculated pattern is obtained. Sample dependent parameters (such as the lattice parameters, atomic co-ordinates, fractional occupancies, temperature factors and background) are refined simultaneously with instrumental parameters (such as zero point and peak

shape). Critically, feedback is given during the refinement process as to how well the fit is progressing.<sup>6</sup>

The residual  $S_y$ , is the quantity that is measured during refinement:

$$S_y = \sum_i w_i (y_i(\text{obs}) - y_i(\text{calc}))^2 \quad \text{Eqn. 2.3.}$$

where  $w_i = 1/y_i(\text{obs})$ ,  $y_i(\text{obs})$  = observed intensity at step  $i$ , and  $y_i(\text{calc})$  = calculated intensity at step  $i$ , summed for all data points.

The Rietveld method is not a means of structure *solution* as such, but rather a structure *refinement* technique: hence a good starting model is required. Care must be exercised since the best-fit will depend on the adequacy of the model (the model must contain the parameters required to model the actual structure) and whether the true minimum, rather than a local minimum has been reached. Goodness of fit may be estimated by the use of 'R-factors' such as R-pattern:

$$R_p = \frac{\sum_i |y_i(\text{obs}) - y_i(\text{calc})|}{\sum_i y_i(\text{obs})^2} \quad \text{Eqn. 2.4.}$$

or, R-weighted pattern:

$$R_{wp} = \left\{ \frac{\sum_i w_i (y_i(\text{obs}) - y_i(\text{calc}))^2}{\sum_i w_i (y_i(\text{obs}))^2} \right\}^{\frac{1}{2}} \quad \text{Eqn. 2.5.}$$

The latter better reflects the progress of the refinement because the numerator is the residual being minimised.

The strategy for refinement (once a model has been decided on) is to refine parameters systematically, with the ones affecting the biggest change being varied first. A typical refinement may proceed with the zero point and lattice parameters being refined first, followed by the background and peak shape before the atomic co-ordinates, fractional occupancies and temperature factors. Refinement cycles are then made until a acceptable fit is achieved.

### 2.1.3. Quantitative X-ray Methods<sup>7</sup>

The intensity of each peak in the powder diffractogram is proportional to the quantity of diffracting material present, save for an absorption correction. The relationship between the intensity and absorptive properties have been investigated, from which a formula<sup>8</sup> is derived:

$$I_1 = \frac{K_1 x_1}{\rho_1 [x_1 (\mu_1^* - \mu_m^*) + \mu_m^*]} \quad \text{Eqn. 2.6.}$$

Where  $I$  is the intensity of an X-ray from a plane;  $K_1$  depends on the nature of component one;  $\rho$  is the linear absorption coefficient;  $x_1$  is the weight of fraction one;  $\mu_1^*$  is the density of component one and  $\mu_m^*$  is the density of component  $m$ .

In the general case the absorption coefficient is unknown and so an internal standard  $s$ , is added in known amount to the sample. The volume of fractions of the unknown and internal standard are  $f_1'$  and  $f_s$ , with the volume of component one in the original sample being  $f_1$ , thus:

$$I_1 = \frac{K_1 f_1'}{\mu}, \quad I_s = \frac{K_s f_s}{\mu} \quad \text{Eqn. 2.7.}$$

$$x_1' = \frac{K_s \rho_1 x_s}{K_1 \rho_s} \cdot \frac{I_1}{I_s} = k' \cdot \frac{I_1}{I_s} \quad \text{Eqn. 2.8.}$$

The weight of  $x_1$  is sought through:

$$x_1 = \frac{x_1'}{1 - x_s'} \quad \text{Eqn. 2.9.}$$

When Equations 2.8. and 2.9. are combined we have:

$$x_1 = \frac{k'}{1 - x_s'} \cdot \frac{I_1}{I_s} = k \cdot \frac{I_1}{I_s} \quad \text{Eqn. 2.10.}$$

It can be seen that when the internal standard is added in a constant proportion  $x_s$ , the concentration of fraction one is a linear function of the intensity ratio  $I_1/I_s$ .

## 2.2. Nuclear Magnetic Resonance Spectroscopy<sup>9</sup>

When a sample is placed in a magnetic field a bulk macroscopic magnetisation of the nuclei occurs. This may then be perturbed from its equilibrium position by a pulse of radio frequency radiation. The response of the system is then monitored (rather than directly measuring the absorption or emission of energy as in other spectroscopies).

Consider first a  $^1\text{H}$  NMR experiment. The proton's nuclear spin has a magnetic moment associated with it that will interact with the applied magnetic field. The proton has a spin ( $I = 1/2$ ) which generates two energy levels ( $\alpha$  and  $\beta$ ) in a magnetic field (due to the Zeeman interaction). These energy levels are separated by a value  $\Delta E$ , that is field dependent:

$$\Delta E = \frac{h\gamma B_0}{2\pi} \quad \text{Eqn. 2.11.}$$

where  $\gamma$  is the magnetogyric ratio and  $B_0$  is the magnitude of the applied static magnetic field.

The magnetogyric ratio is the proportionality constant that relates the observation frequency for a particular nucleus to the applied magnetic field. The observation frequency can be expressed in terms of the magnetogyric ratio and the applied magnetic field:

$$\nu = \frac{\gamma B_0}{2\pi} \text{ or } \omega = \gamma B_0 \quad \text{Eqn. 2.12.}$$

where  $\nu$  is the resonant frequency in Hertz and  $\omega$  is the resonance frequency in radians/second.

Different observation frequencies are observed on different spectrometers due to variations in  $B_0$ . The Boltzmann equation (Equation 2.13.) describes the ratio of population of the two states,  $\alpha$  and  $\beta$ , which are unequal:

$$\frac{N_\beta}{N_\alpha} = \exp\left(\frac{-\Delta E}{kT}\right) \quad \text{Eqn. 2.13.}$$

where  $N_\beta$  is the population of the upper state and  $N_\alpha$  is the population of the lower state:

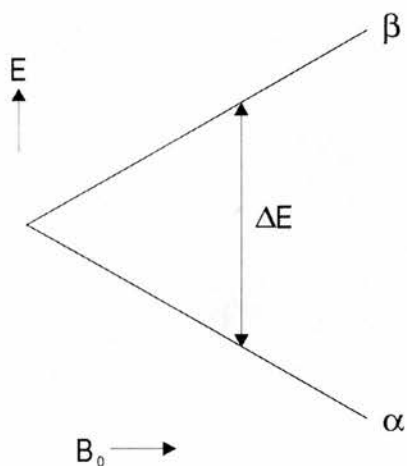


**Figure 2.2.** The energy level diagram for a nucleus with spin  $I = 1/2$  in a magnetic field  $B_0$ .

The difference in population is very small however, of the order of 1-in- $10^5$ , and depends on the field and the nuclear species being observed. (NMR is therefore intrinsically not a very sensitive method.)

The behaviour of the bulk magnetisation  $M$  (the sum of the magnetisation of the individual spins) can be represented by vector diagrams. Before perturbation the bulk magnetisation is aligned with the applied static field, which is defined as  $z$ :

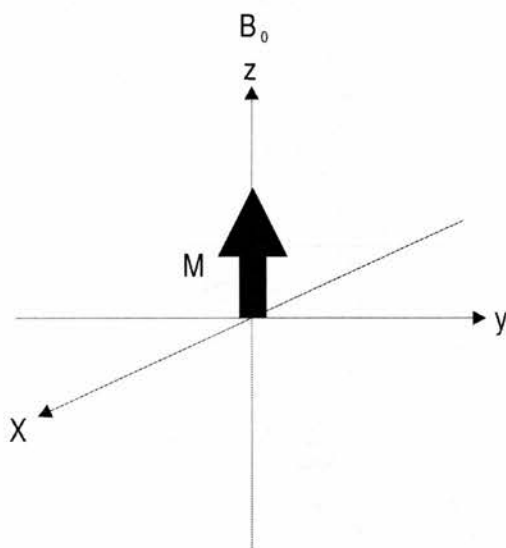


**Figure 2.3.** The behaviour of the bulk magnetisation  $M$ , at equilibrium.

If this magnetisation were perturbed from the  $z$ -direction there would be a force exerted on  $M$  by  $B_0$ . This force, or torque, will cause  $M$  to precess around  $B_0$  at a frequency of  $\gamma B_0$  radians/second or  $\gamma B_0/2\pi$  Hertz (c.f. a gyroscope in a gravitational field). This is the Larmor precession and for typical nuclei are in the range 10 – 100 Hz—radio frequencies:

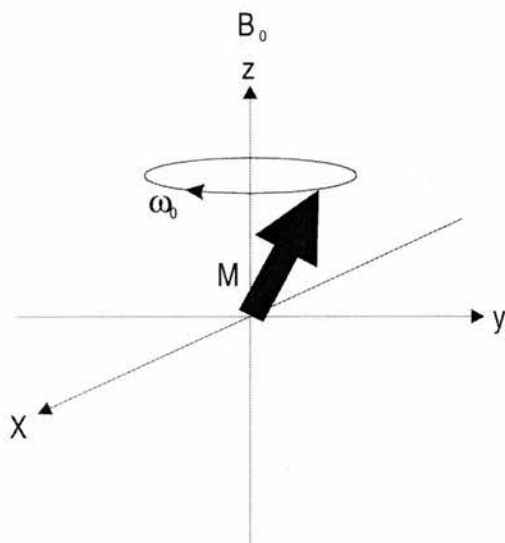


**Figure 2.4.** The behaviour of the bulk magnetisation  $M$ , after perturbation by a pulse of r.f. energy.

Thus, if the magnetisation can be moved away from equilibrium to an excited state then precession will occur. This may be detected as an induced oscillating current in a coil placed in the  $xy$ -direction—the NMR signal.

The perturbation is produced by a second magnetic field  $B_1$ , which oscillates at the appropriate radio frequency. It is produced from a current in a coil wound perpendicular to  $B_0$ , defined to be the  $x$ -axis (and may be the same coil in which the signal is received). This linear field oscillation, along the  $x$ -axis, is equivalent to two counter rotating field vectors in the  $xy$ -plane:

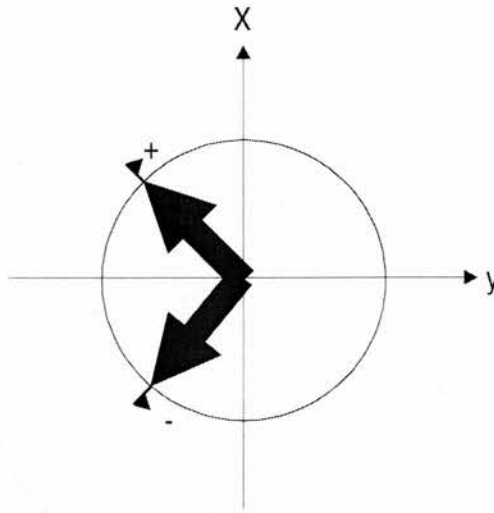


**Figure 2.5.** The linear field oscillation generated in the  $xy$ -plane is equivalent to two rotating field vectors.

Imagine the excitation frequency is equal to the nuclear precession frequency:

$$\omega_1 = \omega_0 = \gamma B_0 \quad \text{Eqn. 2.14.}$$

The field  $B_1$ , interacts with the magnetisation  $M$ , to produce a torque that moves the magnetisation towards to  $xy$ -plane. The magnetisation continues to precess around  $B_0$  at frequency  $\gamma B_0$  while now also precessing around  $B_1$  at frequency  $\gamma B_1$ . The final position of the magnetisation will depend on the length of time  $t_p$ , for which the radio frequency  $B_0$ , is applied. The 'tip' angle  $\theta$ , can be calculated as:

$$\theta = \gamma B_1 t_p \quad \text{Eqn. 2.15.}$$

$B_1$  is chosen to be large to tip the magnetisation from  $z$  to the  $xy$ -plane in a few microseconds.

If we adopt a rotating reference frame where  $z'$ -axis is the static magnetic field direction and  $x'$  and  $y'$  rotate about the  $z'$ -axis at a frequency  $\gamma B_0$ , the angular component due to the precession induced by  $B_0$  is, in effect, removed.

## 2.2.1. NMR in the Solid State<sup>10</sup>

### 2.2.1.1. Sources of Line Broadening

For spin  $I = 1/2$  nuclei (e.g.  $^1\text{H}$ ,  $^{13}\text{C}$ ) there are only two possible sources of significant line broadening: the effect of nearby magnetic nuclei that generate dipole-dipole interactions and chemical shift anisotropy (CSA) that is not averaged to its isotropic value by the tumbling of molecules as in the liquid phase.

Dipolar broadening is most significant in solids containing  $^1\text{H}$  and  $^{19}\text{F}$  but is generally present. At the nucleus I, the local field  $B_{\text{loc}}$ , generated by another nucleus S, will be:

$$B_{\text{loc}} = \pm \mu_S r_{\text{IS}}^{-3} (3 \cos^2 \theta_{\text{IS}} - 1) \quad \text{Eqn. 2.16.}$$

where  $\mu_S$  is the magnetic moment of S,  $r_{\text{IS}}$  is the internuclear distance and  $\theta$  is the angle between the internuclear vector and the  $B_0$  field. The plus/minus arises because the spins generating the local field may be orientated with or against the applied field. In general however, it is the chemical shift anisotropy that is the most significant in the systems reported here. The chemical shift is produced by the electrons that shield the nucleus from the applied magnetic field. CSA results from the applied magnetic field because the electron distribution has a definite directional character that is taken on by the chemical shift. The chemical shift depends upon  $3 \cos^2 \theta - 1$  where  $\theta$  is the angle between the magnetic field and the principal axis about which the chemical shift is defined. In a powdered sample CSA results in line-broadening because the crystallites are randomly orientated within the applied field.

### 2.2.1.2. Overcoming Line Broadening: Magic Angle Spinning (MAS)

In solid materials the dipolar coupling and chemical shift anisotropy contain an angular dependence  $(3 \cos^2 \theta - 1)$ . Thus, we can produce narrower lines by making use of the fact that  $3 \cos^2 \theta - 1 = 0$  when  $\theta = 54^\circ 44'$ : the magic angle. In polycrystalline samples the material must also be spun to average out orientation effects. The rate of rotation must be of the order of the CSA linewidth.

### 2.2.1.3. Spin > 1/2 Nuclei

Nuclei with  $I > 1/2$  possess a quadrupole due to the interaction of the nuclear spin with a non-spherically symmetric electric field gradient at the nucleus. This generates two effects: firstly, quadrupolar splitting: the NMR signal may be split into several components by the quadrupolar interaction; secondly, this interaction may also provide a very efficient relaxation mechanism.

Very many nuclei are quadrupolar, including  $^{11}\text{B}$  and  $^{27}\text{Al}$  which have  $I = 3/2$  and  $I = 5/2$ , respectively. Figure 2.6. illustrates the effect of the quadrupolar interaction on the Zeeman splitting in  $^{11}\text{B}$ . The  $+1/2 \leftrightarrow -1/2$  transition is unaffected by the first order quadrupolar interaction (both are shifted by the same amount in the same direction) while the other two allowed transitions are usually too broad and shifted too far from resonance to be observed directly.

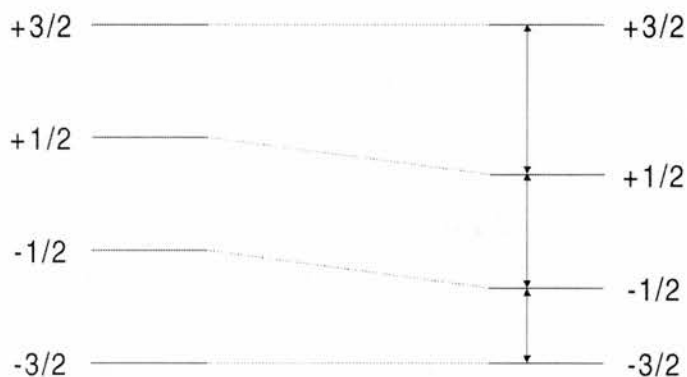


**Figure 2.6.** Diagram representing the energy levels in a nucleus of  $I = 3/2$  due to the Zeeman and first order quadrupolar interactions.

The line shape due to the  $+1/2 \leftrightarrow -1/2$  transition is distorted and shifted due to the second order quadrupolar interaction. This may be minimised by working at high fields or by spinning the sample at more than one angle (which has been done either by switching the angle during the experiment or spinning at two angles simultaneously with a rotor-within-a-rotor).<sup>11</sup> These approaches to deriving solid state spectra of quadrupolar nuclei are highly demanding in terms of spectrometer design. More recently a method utilising pulse sequences to obtain the same resolution has been devised, multiple quantum, or MQ MAS NMR.<sup>12</sup> Although detailed understanding of this method is beyond the scope of this thesis, 2-D  $^{11}\text{B}$  and

<sup>27</sup>Al MQ MAS NMR spectra are presented that indicate the power of the technique to resolve different boron environments.

## 2.3. Statistical Experimental Design<sup>13</sup>

### 2.3.1. Response Surface Designs

The purpose of the methods discussed is to adjust the factor levels,  $x_1, x_2, \dots, x_k$  (where  $x_1$  may be temperature,  $x_2$ , amount of reagent A), to give the best response. This may be the average size of crystallite in a sample, or the intensity of an X-ray diffraction line. The true level of the response, for a combination of factors, is denoted  $\eta$ . However, the measured response, subject to experimental error ( $\sigma^2$ ) is  $y$ . A function links the quantitative factors to the response:

$$\eta = \phi(x_1, x_2, \dots, x_k) \quad \text{Eqn. 2.17.}$$

It is convenient to represent this relation pictorially; if a set of experiments examines two factors the results may be plotted onto a response surface. Such a surface can be described by a polynomial with constants  $\beta_0, \beta_1 \dots, \beta_k$ , as:

$$\eta = \beta_0 + \beta_1 x_1 + \beta_2 x_2 + \beta_{11} x_1^2 + \beta_{22} x_2^2 + \beta_{12} x_1 x_2 + \dots \quad \text{Eqn. 2.18.}$$

Successive terms are said to be of degree 0, 1, 2, and so on, depending on the number of variables multiplied together. Thus,  $\beta_0$  multiplies 1 and is degree zero;  $\beta_1$  and  $\beta_2$  multiply  $x_1$  and  $x_2$  respectively and are degree one. We may say that  $\beta_1$  and  $\beta_2$  measure the *linear effects*,  $\beta_{11}$  and  $\beta_{22}$  measure the *quadratic effects* while  $\beta_{12}$  measures the *linear by linear interaction*. Taking terms up to the first degree we have the equation of a straight line, at the second degree a parabola. The wider the range of  $x_1$  and  $x_2$  the greater the number of terms required to obtain a good fit to the experimental data. In general the second degree polynomial (which is most commonly used in practice) is:

$$\eta = \beta_0 + \sum_i \beta_i x_i + \sum_i \beta_{ii} x_i^2 + \sum_i \sum_{j \neq i} \beta_{ij} x_i x_j \quad \text{Eqn. 2.19.}$$

The position of a maximum within the range considered can then be estimated by differentiating the fitted expression and equating the derivative to zero. If, for example, terms to the second degree are considered and  $b_0$ ,  $b_1$  and  $b_{11}$  were the least squares estimates of  $\beta_0$ ,  $\beta_1$  and  $\beta_{11}$ , the fitted equation would be:

$$Y = b_0 + b_1x_1 + b_2x_2 + b_{11}x_1^2 + b_{22}x_2^2 + b_{12}x_1x_2 \quad \text{Eqn. 2.20.}$$

where  $Y$  is the value calculated from the fitted equation. Differentiating both sides of this equation and equating to zero we have:

$$\frac{dY}{dx_1} = b_1 + 2b_{11}x_1 + b_{12}x_2 \quad \text{Eqn. 2.21.}$$

The values of the coefficients  $b$ , can be calculated from the experimental data, thus:

$$b = \frac{\sum xy}{\sum x^2} \quad \text{Eqn. 2.22.}$$

The quadratic equation can then be solved and the value  $x_1$  pertaining to a maximum found.

### 2.3.2. Experiment Structure

A treatment structure, or the pattern of factors' levels across a set of experiments, is also required:  $2^n$  and  $3^n$  factorial designs are commonly used. With the former we examine  $n$  factors at two levels, high and low (and conduct  $2^n$  experimental runs). This does not allow estimation of quadratic terms in the second degree polynomial because with two levels there can be no information about the slope—we have to assume a linear relationship. The  $2^n$  design simply gives information about the gradient of the surface in all directions; moreover, for more than four variables it becomes wasteful, using many more combinations than are necessary for the estimation of the linear surface equation. Equation 2.19. can be employed with  $3^n$  designs but these suffer more from the increasing number of experiments required and are so best kept for when more is known about the position of the optimum point. A third composite design has been developed based on the  $2^n$  structure, the components being:

1.  $2^n$  structure with  $\pm 1$  for each factor
2. origin observations: (0, 0, ..., 0)
3. axial observations: ( $\pm\alpha$ , 0, ..., 0), (0,  $\pm\alpha$ , ..., 0), (0, 0, ...,  $\pm\alpha$ )

For three factors this can be expressed graphically by points on a cube, each corner, for example, corresponding to a high or low value in the design with an experiment being carried out for each of the fifteen points on the diagram. The principal advantage of this design is that the work can progress in logical stages as the first eight runs correspond to the  $2^n$  factorial design and may be analysed separately.

## 2.4. References

1. G. F. Liptrot, J. J. Thompson and G. R. Walker, *Modern Physical Chemistry*, Bell and Hyman, London, 4th edn., 1986, ch. 13, p.174.
2. M. M. Woolfson, *An Introduction to X-ray Crystallography*, Cambridge University Press, Cambridge, 2nd edn., 1997, ch. 3, pp. 50–75.
3. H. L. Monaco, in *Fundamentals of Crystallography*, ed. C. Giacovazzo, Oxford University Press, Oxford, 1st edn., 1992, ch. 4, pp. 229–318.
4. Powder Diffraction File, Sets 1–49, International Centre for Diffraction Data, Newtown Square, 1999.
5. H. M. Rietveld, *Acta Crystallogr.*, 1967, **22**, 151; *J. Appl. Crystallogr.*, 1969, **2**, 65.
6. R. A. Young, in *The Rietveld Method*, ed. R. A. Young, Oxford University Press, Oxford, 1st edn., 1993, ch. 1, pp. 1–38.
7. H. P. Klug and L. E. Alexander, *X-ray Diffraction Procedures for Polycrystalline and Amorphous Materials*, John Wiley and Sons, New York, 1st edn., 1954, ch. 7, pp. 410–439; H. Eyring, *Physical Chemistry*, ed. W. Jost, Academic Press, New York, 1st edn., 1970, vol. 10, pp. 50–57.
8. L. Alexander and H. P. Klug, *Anal. Chem.*, 1948, **20**, 886.
9. J. K. M. Sanders and B. K. Hunter, *Modern NMR Spectroscopy*, Oxford University Press, Oxford, 2nd edn., 1993.
10. C. A. Fyfe and R. E. Wasylshen, in *Solid State Chemistry Techniques*, eds. A. K. Cheetham and P. Day, Oxford University Press, Oxford, 1st edn., 1987, ch. 6, pp. 190–230.

11. K. T. Mueller, B. Q. Sun, G. C. Chingas, J. W. Zwanziger, T. Terao and A. Pines, *J. Magn. Reson.*, 1990, **86**, 270.
12. A. Medek, J. S. Harwood and L. Frydman, *J. Am. Chem. Soc.*, 1995, **117**, 12779; S. P. Brown and S. Wimperis, *J. Magn. Reson.*, 1997, **128**, 42.
13. W. P. Gardiner, *Statistical Analysis Methods for Chemists*, Royal Society of Chemistry, Cambridge, 1st edn., 1997; R. Mead, *The Design of Experiments*, Cambridge University Press, Cambridge, 1st edn., 1988; *The Design and Analysis of Industrial Experiments*, ed. O. W. Davies, Oliver and Boyd, Edinburgh, 2nd edn., 1956.

## Chapter Three

# Boron Substitution in Microporous Materials

### 3.1 Abstract

The hydrothermal synthesis of crystalline solids from gels of composition  $\text{Al}_2\text{O}_3\text{-P}_2\text{O}_5\text{-B}_2\text{O}_3\text{-H}_2\text{O}$  was investigated in the presence of two families of primary amines: isopropylamine, N-isopropylethylenediamine, N'-isopropyl-diethylenetriamine and *trans*-1,4-diaminocyclohexane, *trans*-1,2-diaminocyclohexane, *cis*-1,2-diaminocyclohexane. Selected materials were investigated further by X-ray diffraction, MAS NMR and compositional analysis. Phase pure products were prepared but only low boron contents were recorded in the solids (less than 0.13 wt%). The effects of temperature, time and aluminium-to-phosphorus ratio, on crystallite size, was examined efficiently in a statistically designed set of experiments for a phase templated by *trans*-1,4-diaminocyclohexane. Crystallites of sufficient size for conventional single crystal X-ray diffraction were synthesised and the material was found to be related to a known phase: of layer stoichiometry  $[\text{Al}_3\text{P}_4\text{O}_{16}^{3-} \cdot 1.5(\text{H}_2\text{N}-\text{C}_2\text{H}_4-\text{NH}_2)^{2+}]$  of Jones *et al.*<sup>1</sup>

Designed synthesis in the  $\text{Al}_2\text{O}_3\text{-B}_2\text{O}_3\text{-CaO-H}_2\text{O}$  system were performed in an effort to reproduce the literature synthesis of an aluminoborate with interesting properties reported by Jianhua *et al.*<sup>2</sup> Good quality microporous solids were prepared that gave similar but not identical diffraction patterns to those reported, and suggest that the literature material was not phase pure.

### 3.2 Introduction

The aim of this work was to synthesis boro-aluminophosphate solids and determine (a) the role boron plays in the crystallisation process and (b) the solids' structure. Optimisation of synthesis conditions was also to be carried out. An aluminoborate material B-C7, first reported by Jianhua *et al.*<sup>2</sup> was also to be prepared.

The materials studied here are all microporous zeotypes but it will be useful to look at their parent materials, the zeolites, first.

### 3.2.1. Zeolites

Zeolites have an open structure that may reversibly sorb and desorb water. It was this that led the Swedish mineralogist Cronstedt,<sup>3</sup> who first observed intumescence in stilbite, to name them after the Greek, ζεῖν—boil and λίθος—stone. They are a class of crystalline tectoaluminosilicate materials, related to feldspars and feldspathoids, whose structure contains TO<sub>4</sub> tetrahedra, each apical oxygen being shared with an adjacent tetrahedron. It is possible for the tetrahedra to link by two, three or four corners, and with T–O–T angles of *ca.* 125° to *ca.* 180° making a variety of structures possible.

In nature large zeolite specimens are typically formed in basaltic vugs and cavities; they are also created in sedimentary tuff deposits from the recrystallisation of volcanic material in mineralising solutions; geothermal action also creates zeolites. The minerals' structures depend on depth and temperature of the deposit.

Aluminosilicate zeolites can be represented generally as:



Non-framework cations    Framework    Sorbed phase

The framework is anionic and consists of [SiO<sub>4</sub>]<sup>4-</sup> and [AlO<sub>4</sub>]<sup>5-</sup> tetrahedra (the primary building units) with a metal-to-oxygen atom ratio of two. The overall charge on the framework is equal to the number of tetrahedral aluminium atoms so a corresponding number of cations are required for charge balance. These cations have access to the pore system and are incorporated into the structure at synthesis, yet can be exchanged later. The third structural element is the sorbed phase, either water or an organic, which plays an important role in the synthesis of the particular phase. Following crystallisation this species can be removed, by heating or under reduced external pressure, to leave the framework structure intact.

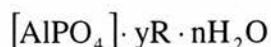
Although the framework composition may vary considerably depending on synthesis conditions,<sup>4</sup> or from later modification, in zeolites the silicon-to-aluminium ratio must always be greater than one. This was rationalised by Loewenstein<sup>5</sup> in terms of an Al–O–Al avoidance rule on the basis that having adjacent  $[\text{AlO}_2]^-$  units would mean having adjacent negative charges and so would be unfavourable. Recent theoretical studies<sup>6</sup> rationalise the rule in terms of unfavourable energetics. At higher silicon-to-aluminium ratios the number of non-framework cations is reduced (along with the number of acid sites, although their relative strength increases). The sorbative characteristics become hydrophobic, five-membered ring formation is promoted and the materials become more hydrothermally stable.

The structure of these materials can be described in terms of secondary (e.g. 4 and 6 membered rings) and tertiary (e.g. various cages) building units<sup>7</sup>. When viewed along one of the crystallographic directions the structures appear as two-dimensional three connected nets; these may be linked through various structural units. The arrangement of the layers, the stacking sequence, is used to classify zeolite structures.

As stated before, boron has been found to substitute for aluminium, and rarely silicon, in zeolites to form boralites, giving solids of mild Brønsted acid strength.

### 3.2.2. Zeotypes

Work at Union Carbide yielded a new family of microporous solids in 1982,<sup>8</sup> the aluminophosphates, or  $\text{AlPO}_4$ s. These materials can form three-dimensional structures analogous to aluminosilicates (such as  $\text{AlPO}_4$ -37—faujasite and  $\text{AlPO}_4$ -34—chabazite) as well as novel ones ( $\text{AlPO}_4$ -5, for example). Aluminophosphate materials provide a rich seam of novel structures<sup>9</sup> that can be represented thus:



The framework is comprised of  $[\text{AlO}_2]^-$  and  $[\text{PO}_2]^+$  units which strictly alternate to give a neutral structure. This prohibits the formation of five-rings although aluminium can, on occasion, adopt five or six co-ordination. Aluminophosphates can

be substituted<sup>10</sup> by a range of heteroatoms M, to form MAPO or by silicon (SAPO) or both (MAPSO). Loewenstein's rule can be extended to prohibit P–O–P, P–O–Si, M–O–Al, and M–O–M linkages.

In addition to fully tetrahedrally-co-ordinated structures aluminophosphate may form in one-dimensional chains<sup>11</sup> and two-dimensional layers.<sup>12</sup> More than twelve layered materials have been reported to date<sup>13</sup> and yet there are only six structurally unique materials, all with one of just two unique layer stoichiometries:  $[\text{Al}_3\text{P}_4\text{O}_{16}]^{3-}$  and  $[\text{Al}_2\text{P}_3\text{O}_{12}\text{H}_x]^{(3-x)-}$ ,  $x = 1 - 2$ .

Boron has been found to substitute for aluminium in  $\text{AlPO}_4$  prepared with triethylamine as the template at concentrations of  $\text{B}_{0.05}\text{Al}_{0.96}\text{PO}_4$ .<sup>14</sup> In this case the boron has been shown by  $^{11}\text{B}$  MAS NMR to be in tetrahedral co-ordination in as-prepared and calcined materials.

If all the aluminium in the  $\text{AlPO}_4$  were to be replaced by boron then in principle a new class of material would result—the borophosphates. There are intermediate compounds of the system  $\text{M}_x\text{O}_y\text{--B}_2\text{O}_3\text{--P}_2\text{O}_5\text{--H}_2\text{O}$  that typically contain  $\text{BO}_4$  species. To date a number of materials have been synthesised containing various metals M, both hydrothermally<sup>15</sup> and by solid state reactions.<sup>16</sup> The first metal borophosphate with an open framework structure ( $\text{CoB}_2\text{P}_3\text{O}_{12}(\text{OH})\cdot\text{C}_2\text{H}_{10}\text{N}_2$ ) was synthesised by Sevov<sup>17</sup> and contains 4.86 wt% boron in tetrahedral co-ordination.

There are also examples where framework solids are prepared containing boron and aluminium such as that reported by Jianhua *et al.*; the structure of this material is unknown, but could be related to the known phase jeremejerite. The solid was synthesised in six days at 200 °C from a gel of composition  $0.6\text{CaO}\cdot 1.0\text{Al}_2\text{O}_3\cdot 6.0\text{B}_2\text{O}_3\cdot 0.5\text{TEAOH}\cdot 150\text{H}_2\text{O}$  (TEAOH = tetraethylammonium hydroxide). The solid had composition  $\text{Al}_2\text{B}_{19}\text{CaO}_{32}\cdot 4.3\text{H}_2\text{O}$ , organic template being found within the material's pores. These were estimated to be between 5 – 6 Å in diameter from adsorption measurements. Two bands in the IR spectrum were assigned to trigonal and tetrahedral boron species (1298 – 1384  $\text{cm}^{-1}$  and 1071 – 1101  $\text{cm}^{-1}$ , respectively). The framework was reported to be stable to heating until 733 °C.

### 3.3. Experimental

#### 3.3.1. Boro-aluminophosphate Synthesis

Materials templated by two families of three amines were studied in depth. The first was the diaminocyclohexanes: *trans*-1,4-, *trans*-1,2- and *cis*-1,2-; the second comprised isopropylamine, N-isopropylethylenediamine and N'-isopropyl-diethylenetriamine:

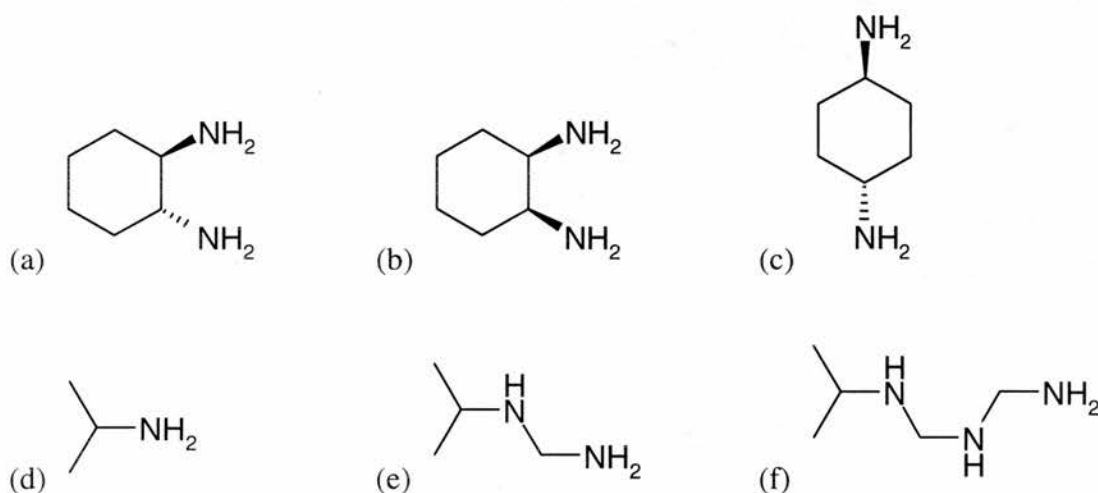


**Figure 3.1.** The structures of (a) *trans*-1,2-diaminocyclohexane, (b) *cis*-1,2-diaminocyclohexane, (c) *trans*-1,4-diaminocyclohexane, (d) isopropylamine, (e) N-isopropylethylenediamine (f) N'-isopropyl-diethylenetriamine.

The BAPOs (boro-aluminophosphates) were synthesized by the sequential addition of aluminium hydroxide (Aldrich), orthophosphoric acid (85 %, Prolabo), trioxoboric(III) acid (99.5 %, Griffin and George) and the amine template to distilled water (St Andrews) using a mole ratio of 0.5 : 1.0 : 0.5 : 0.4 – 0.8 : 40 respectively for the initial experiments. The gel was stirred for fifteen minutes until homogeneous before being transferred to a PTFE-lined, stainless steel autoclave and heated at 160 – 190 °C.

##### 3.3.1.1 Diaminocyclohexane

Preparations were carried out to screen the three isomers of diaminocyclohexane used in this work, as outlined above. As a result of this *trans*-1,4-diaminocyclohexane was selected by further study on the basis of its

powder X-ray diffraction pattern and a series of statistically designed experiments were carried out in an attempt to grow crystals suitable for single crystal diffraction in St Andrews, that is, with a conventional four-circle diffractometer. There are many variables which may effect the outcome of a boro-aluminophosphate synthesis, three have been examined: ratio of aluminate-to-phosphate, heating time and temperature,  $x_1$ ,  $x_2$ ,  $x_3$ , respectively. The set of fifteen experiments which was carried out is given in Table 3.1.; while Table 3.2. shows how each of the factors levels was set.

Trial	FactorLevel		
	$x_1$	$x_2$	$x_3$
1	-1	-1	-1
2	1	-1	-1
3	-1	1	-1
4	1	1	-1
5	-1	-1	1
6	1	-1	1
7	-1	1	1
8	1	1	1
9	-1.215	0	0
10	1.215	0	0
11	0	-1.215	0
12	0	1.215	0
13	0	0	-1.215
14	0	0	1.215
15	0	0	0

**Table 3.1.** Above: shows the set of experiments (trials) that must be done to obtain data for the  $2^3$  composite design. Fifteen experiments were performed with mole ratio of orthophosphoric acid (effectively the  $H_3PO_4 : Al(OH)_3 \cdot xH_2O + B(OH)_3$  ratio), temperature and crystallisation time varied as stated in the table.

Factor	Factor Level						
	-1.215	-1	0	1	1.215	Base Level	Unit
$x_1$ - $H_3PO_4$ , ratio	0.890	1.000	1.500	2.000	2.110	1.500	0.500
$x_2$ - Time, days	1.460	2.000	4.500	7.000	7.540	4.500	2.500
$x_3$ - Temp., °C	157.0	160.0	174.0	187.0	190.0	174.0	13.0

**Table 3.2.** Factor levels ( $-1$  = low and  $+1$  = high) correspond to actual mole ratios, temperatures and times in the  $2^3$  composite design.

### 3.3.1.2. Isopropylamine and derivatives

Isopropylamine, N-isopropylethylenediamine and N'-isopropyl-diethylenetriamine were used to template boro-aluminophosphate materials as described above. Additional preparations were made with isopropylamine in non-aqueous (ethylene glycol) solvothermal synthesis.

### 3.3.2. Aluminoborate Synthesis

Aluminoborate preparations were made by the sequential addition of aluminium hydroxide (Aldrich), trioxoboric(III) acid (99.5 %, Griffin and George), calcium oxide (99.9 %, FSA Laboratory Supplies) and tetraethylammonium hydroxide (35 wt% in water, Aldrich) to distilled water (St Andrews) using the mole ratios given in Tables 3.3. and 3.4. The gels were stirred for fifteen minutes until homogeneous before being transferred to PTFE-lined, stainless steel autoclaves and heated at 200 °C for six days. Since the aim was only to collect qualitative data, a factorial design is all that is required, hence only the first eight experiments in Table 3.1 were performed. The design may be illustrated graphically by plotting the experiments on the corners of a cube (Figure 3.2.). It can be seen then that the origin (0, 0, 0) is at the centre of the cube and each vertex represents a co-ordinate ( $x_1, x_2, x_3$ ) from Table 3.1. The factor levels are set out in Table 3.3.

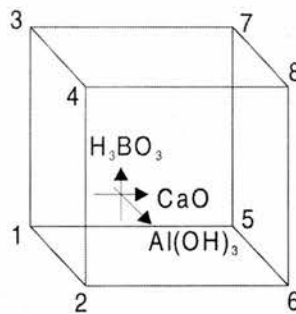


**Figure 3.2.** If the centre of the cube is taken to be the origin (0, 0, 0), each vertex represents a combination of factors ( $x_1, x_2, x_3$ ) taken from Table 3.1.

Factor	Factor Level			Base Level	Unit
	-1	0	1		
$x_1$ - Al(OH) <sub>3</sub> , ratio	1.000	1.500	2.000	1.500	0.500
$x_2$ - H <sub>3</sub> BO <sub>3</sub> , ratio	6.000	9.000	12.000	9.000	3.000
$x_3$ - CaO, ratio	1.200	0.600	1.000	0.600	0.400

**Table 3.3.** Factor levels (−1 = low and +1 = high) correspond to actual mole ratios, temperatures and times in the 2<sup>3</sup> factorial design.

Promising preparations were selected by the presence of low angle diffraction lines, typical of microporous solids. The high and low levels of the factors were adjusted (Table 3.4.) and further preparations carried out.

Factor	Factor Level			Base Level	Unit
	-1	0	1		
$x_1$ - Al(OH) <sub>3</sub> , ratio	0.500	1.000	1.500	1.000	0.500
$x_2$ - H <sub>3</sub> BO <sub>3</sub> , ratio	3.000	6.000	9.000	6.000	3.000
$x_3$ - CaO, ratio	0.600	1.000	1.400	1.000	0.400

**Table 3.4.** Factor levels (−1 = low and +1 = high) correspond to actual mole ratios, temperatures and times in the 2<sup>3</sup> factorial design.

Three further preparations were carried out using a mole ratios of distilled water, aluminium hydroxide, trioxoboric(III) acid, calcium oxide and tetraethylammonium hydroxide (a) 150 : 1.0 : 12.0 : 1.8 : 0.5 respectively; (b) 150 : 1.5 : 12.0 : 1.8 : 0.5 respectively; (c) 150 : 0.0 : 12.0 : 1.8 : 0.5 respectively.

### 3.3.3. Crystallography

Routine phase identification of the materials produced was carried out on one of two Philips X'Pert System powder X-ray diffractometers, in reflectance mode (Bragg-Bentano geometry), using Cu K<sub>α</sub> radiation ( $\lambda = 1.542\text{\AA}$ ) with secondary monochromation and a scintillation counter. Powder samples were placed on an aluminium plate sample holder and data typically collected in 45 minutes over the 2 $\theta$  range 5 – 50°, with a 0.02° step.

Higher resolution data were obtained on a Stoe STADI P high resolution powder X-ray diffractometer in transmission mode (Debye-Scherrer geometry), using primary monochromated Cu K<sub>α1</sub> radiation ( $\lambda = 1.54056\text{\AA}$ ) and a linear position-sensitive detector covering 7° in 2 $\theta$ . Samples were typically mounted in 0.7mm quartz capillaries and data collected in 14 hours over the 2 $\theta$  range 4 – 70° and with a step

size of  $0.02^\circ$ . Quantitative data was collected over the  $2\theta$  range  $7 - 10^\circ$  with a step size of  $0.02^\circ$ ; three sets of data for each preparation were averaged.

Synchrotron powder X-ray diffraction of selected samples was carried out at Station 9.1 of the SRS, CLRC Daresbury Laboratory, Cheshire in Debye-Scherrer geometry. The radiation was monochromated ( $\lambda = 1.000139 \text{ \AA}$ ) and data typically collected over the range  $3 - 60^\circ$  in 12 hours with a scintillation detector.

### 3.3.4. MAS NMR Spectroscopy

Data were collected in St Andrews on a Bruker MSL500 spectrometer using a MAS probe with 4 mm o.d. rotors (of zirconia) for  $^{27}\text{Al}$  and  $^{31}\text{P}$  spectra. External shift reference samples were used:  $\text{Al}(\text{H}_2\text{O})^{3+}(\text{aq})$  and  $\text{H}_3\text{PO}_4(\text{aq})$  for the  $^{27}\text{Al}$  and  $^{31}\text{P}$  spectra respectively.

### 3.3.5. Atomic Absorption Spectroscopy

Analysis of selected samples was performed by atomic absorption spectroscopy at Borax Europe Ltd., Guildford.

## 3.4. Results

### 3.4.1. Boro-aluminophosphate Materials

#### 3.4.1.1. Diaminocyclohexane

The three diaminocyclohexanes (*trans*-1,4-, *trans*-1,2- and *cis*-1,2-),  $M/R = 0.8$ , each gave a product after three days at  $190^\circ\text{C}$ . Heating for longer (six days) had little effect on the products formed except the *trans*-1,2-cyclohexane preparation which began to degrade.

The averaged, absolute intensity data from the statistically designed experiments was processed with MS Excel and the coefficients of Equation 2.20. found. This yielded a quadratic equation that described the factors which produced the largest response (intensity of an X-ray line) which was related to the relative yield of product:

$$Y = 66.61 - 55.17x_1 + 2.63x_2 - 3.36x_3 - 2.93x_1x_2 + 8.83x_1x_3 + 2.55x_2x_3 + 77.44x_1^2 + 58.89x_2^2 + 57.59x_3^2$$

This equation may be solved and the graphs in Figures 3.3. – 3.5. plotted.

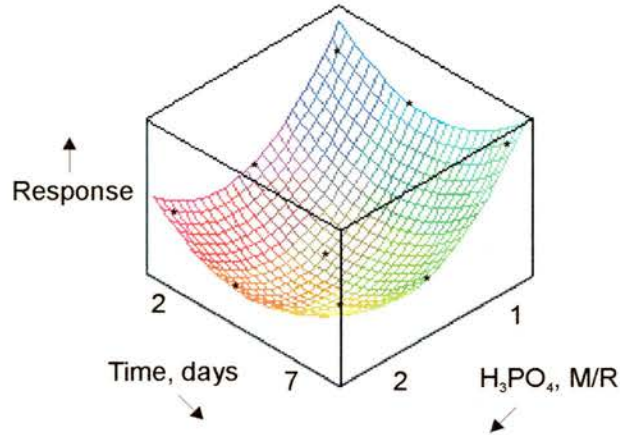


**Figure 3.3.** Plot of Time (days) vs. H<sub>3</sub>PO<sub>4</sub> (mole ratio) against response, showing optimum conditions at 7 days and 0.89 M/R H<sub>3</sub>PO<sub>4</sub>. Experimentally determined responses are marked (\*).

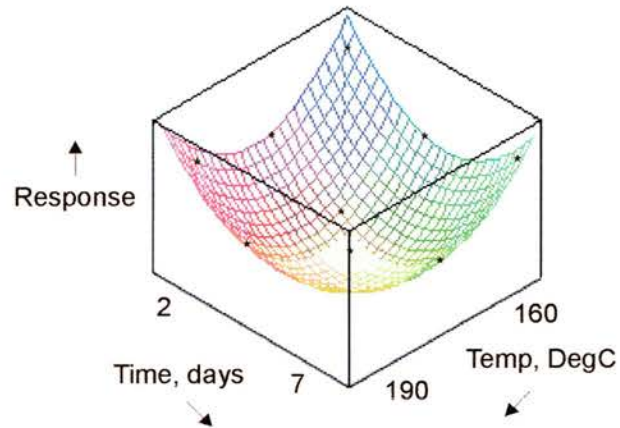


**Figure 3.4.** Plot of Time (days) vs. Temperature (°C) against response, showing optimum conditions at 190 °C and 1.46 days. Experimentally determined responses are marked (\*).

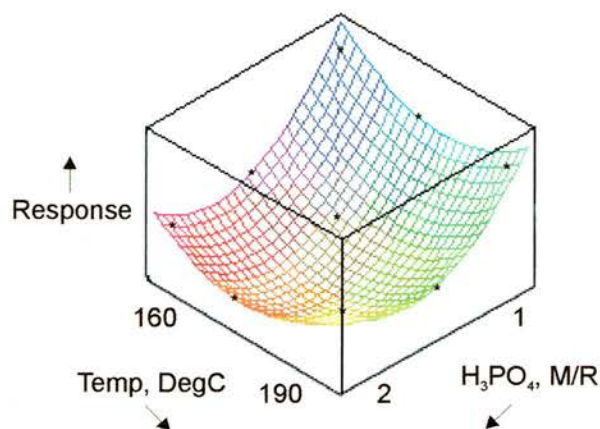


**Figure 3.5.** Plot of Temperature ( $^{\circ}\text{C}$ ) vs.  $\text{H}_3\text{PO}_4$  (mole ratio) against response, showing optimum conditions at  $157^{\circ}\text{C}$  and  $0.89 \text{ M/R } \text{H}_3\text{PO}_4$ . Experimentally determined responses are marked (\*).

Thus it can be seen that the stoichiometry is important (it must be  $0.89\text{H}_3\text{PO}_4$ ), but that temperature and time are less critical: either a higher temperature for a shorter time or else a lower temperature for a longer time appear to yield the greatest quantity of crystalline product.

These preparations were then examined under an optical microscope and single crystals of sufficient size of single crystal X-ray diffraction studies found when the mole ratio of orthophosphoric acid equals one and the gel was heated for two days at  $160^{\circ}\text{C}$ . Single crystal X-ray diffraction data was collected and the unit cell determined to be in the hexagonal space group  $P6_3cm$  with dimensions:  $a = 12.932 \text{ \AA}$  and  $c = 18.254 \text{ \AA}$ . The motif (asymmetric unit) is shown in Figure 3.6.

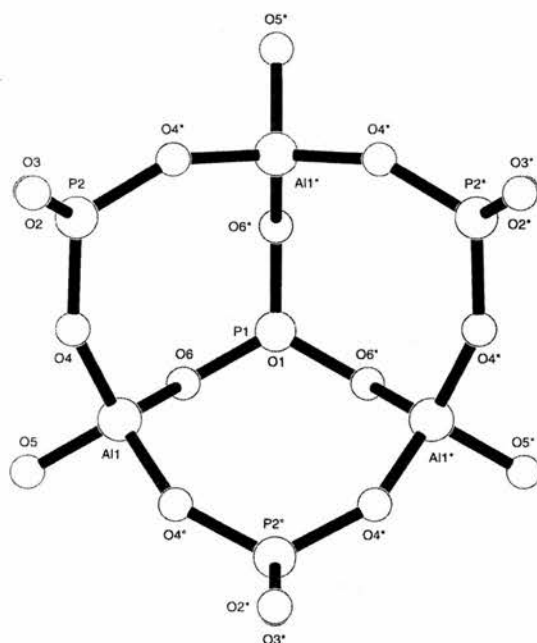


**Figure 3.6.** The motif of the boro-aluminophosphate layer found in the solid crystallised with *trans*-1,4-diaminocyclohexane.

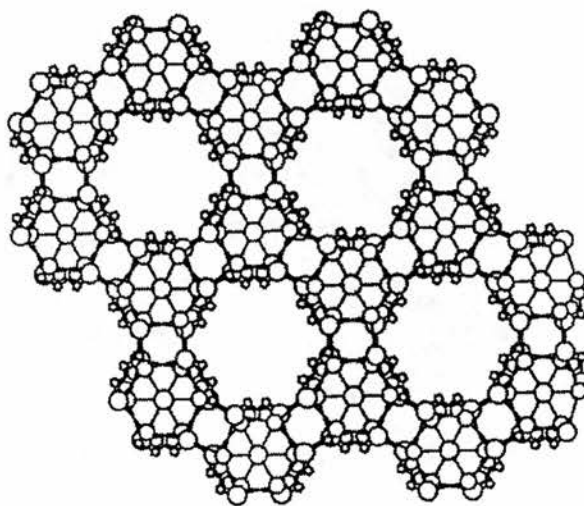


**Figure 3.7.** The boro-aluminophosphate layer, of stoichiometry  $[Al_3P_4O_{16}]^{3-}$ .

Closer examination of the literature data indicated this phase had been previously reported, with 1,4-diaminobutane as the template.

#### 3.4.1.2. Isopropylamine and derivatives

Experiments were carried out with isopropylamine, and then by adding additional ethylamine groups, N-isopropylethylenediamine and N'-isopropyl-diethylene-

triamine. Isopropylamine will direct formation of three different structural phases: phase *A* is produced from the standard gel with 0.8 equivalents of amine (*pH* 6) if heated at 190 °C for six days. Phase *B* forms in half the time under the same conditions if a solvent free synthesis is employed, yet the addition of water to such a preparation causes the third phase, *C* to appear. A non-aqueous synthesis trial was carried out but suffered from reproducibility problems. N-isopropylethylenediamine (*M/R* = 0.8, *pH* 8.5) crystallises a novel phase after six days at 180 °C as does N'-isopropyldiethylenetriamine under the same conditions.

A phase subsequently identified as BA1PO-14A, the pure aluminophosphate form of which was solved by Smith *et al.* from an impurity found in another preparation. Rietveld refinement of the BAPO synchrotron data confirmed this; with a fit of  $R_p = 10.65\%$  and  $R_{wp} = 14.29\%$ .

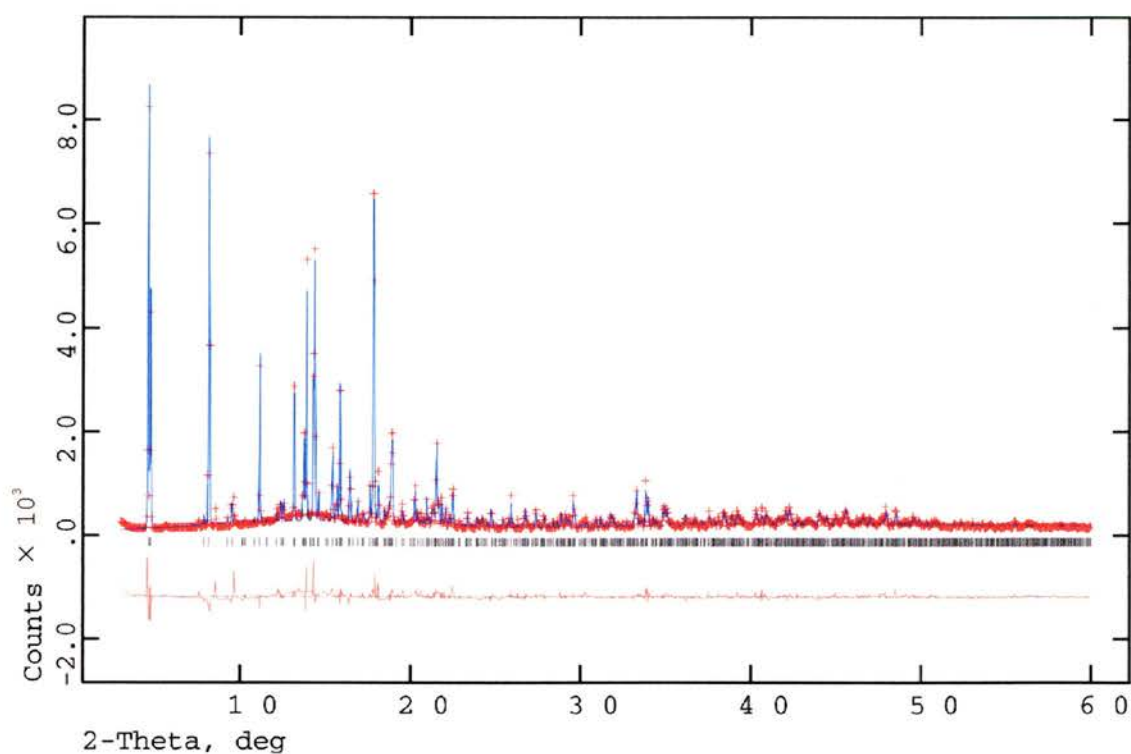


**Figure 3.8.** Rietveld refinement difference plot for BAPO-14A, calculated profile (blue line) and observed profile (red crosses) with difference (red line).

### 3.4.2. Aluminoborate Materials

From the first set of experiments the solid which most closely resembled the literature material was selected on the basis of X-ray profile. This solid came from a gel of composition  $\text{Al}(\text{OH})_3 : 6\text{H}_3\text{BO}_3 : \text{CaO} : 0.5\text{TEAOH} : 150\text{H}_2\text{O}$  (Figure 3.9.). Figure 3.10. shows the results of this second set of experiments which yielded a better material from a gel of composition  $0.5\text{Al}(\text{OH})_3 : 9\text{H}_3\text{BO}_3 : 1.4\text{CaO} : 0.5\text{TEAOH} : 150\text{H}_2\text{O}$ . The XRD pattern for the literature material is given in Figure 3.11. The X-ray diffraction patterns of all sixteen materials are shown in Figures 3.12. and 3.13.

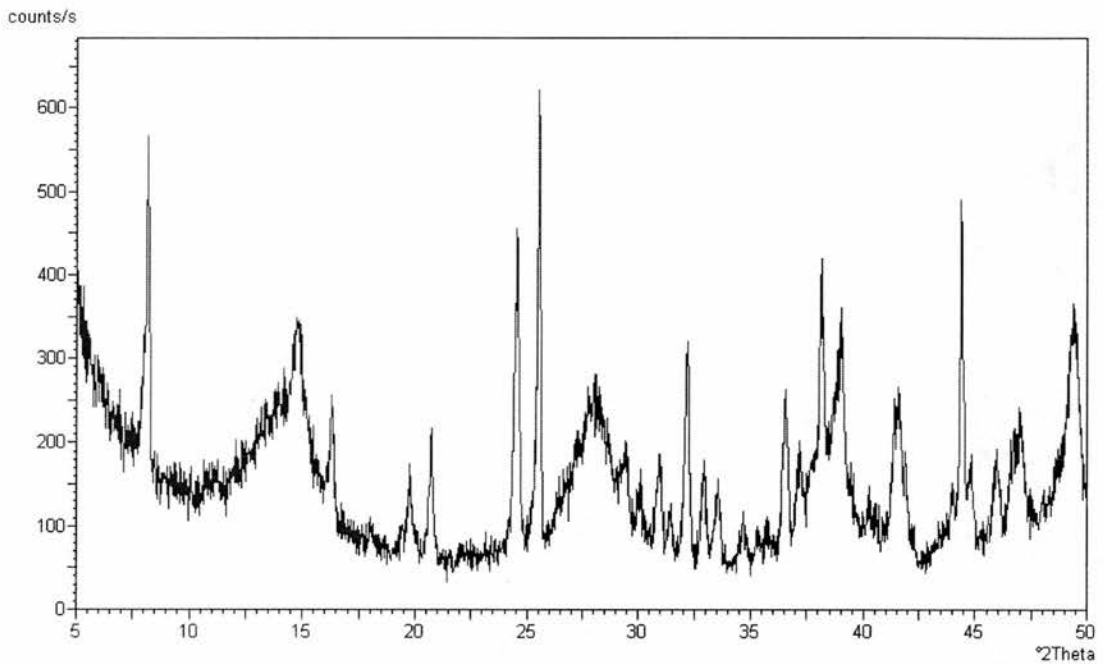


**Figure 3.9.** Aluminoborate from a gel of composition  $\text{Al}(\text{OH})_3 : 6\text{H}_3\text{BO}_3 : \text{CaO} : 0.5\text{TEAOH} : 150\text{H}_2\text{O}$ .

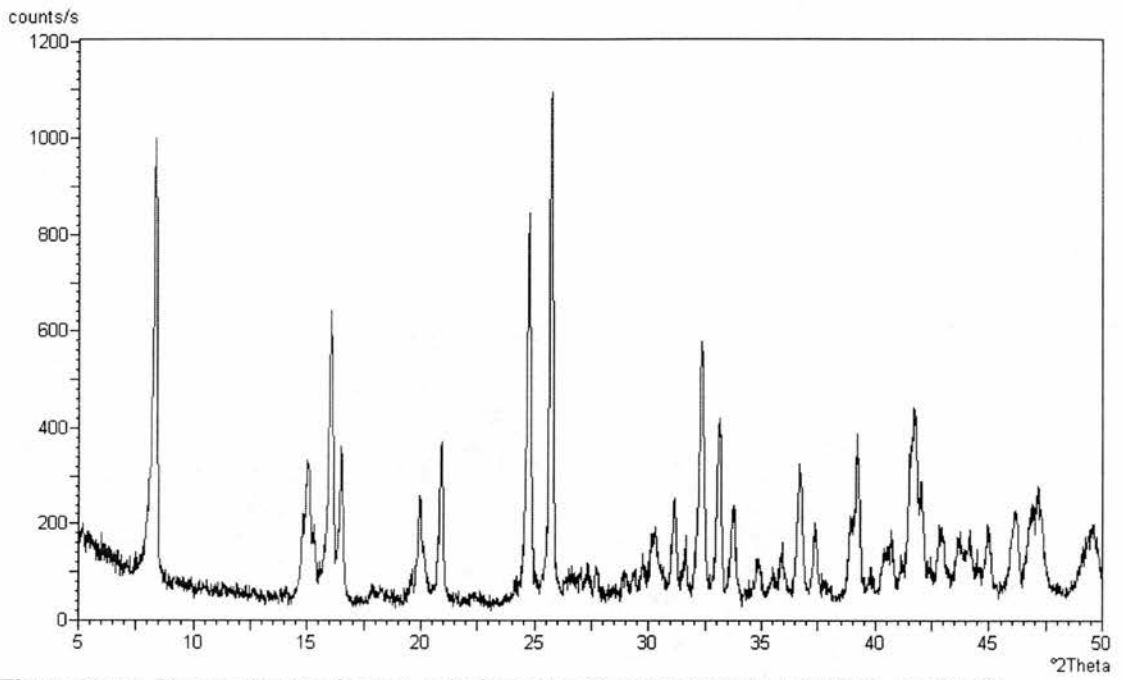


**Figure 3.10.** Aluminoborate from a gel of composition  $0.5\text{Al}(\text{OH})_3 : 9\text{H}_3\text{BO}_3 : 1.4\text{CaO} : 0.5\text{TEAOH} : 150\text{H}_2\text{O}$ .

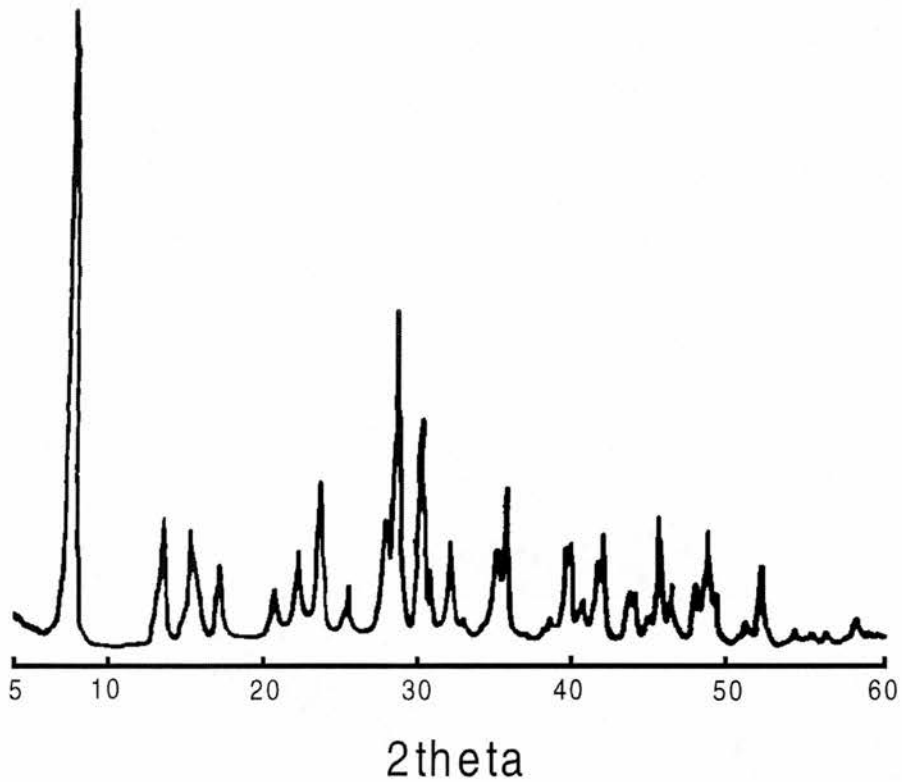


**Figure 3.11.** Aluminoborate material from the literature.

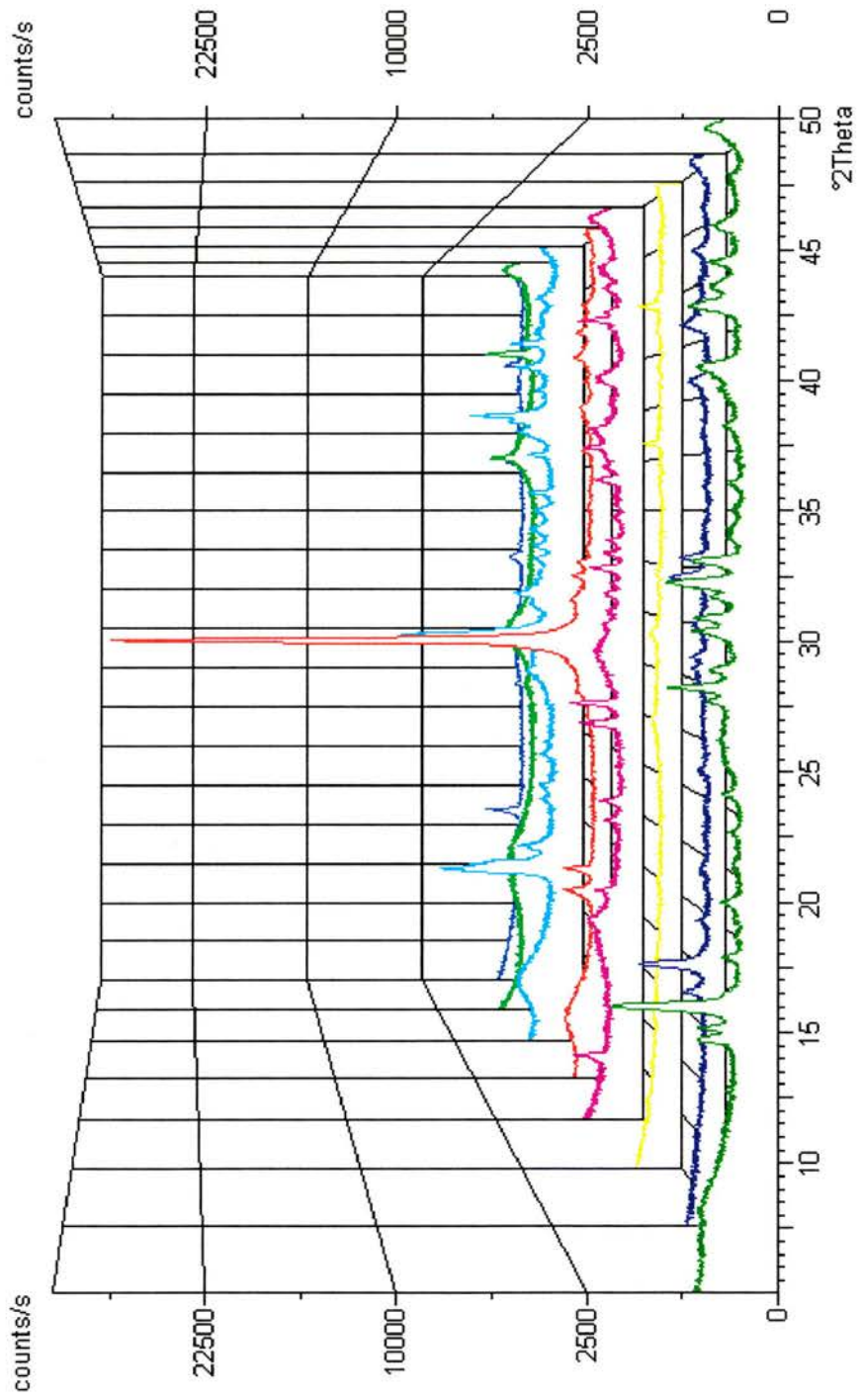


**Figure 3.12.** X-ray diffraction patterns of aluminoborate phases made in experiments 1 (back) to 8 (front). For experimental variables see Table 3.3.

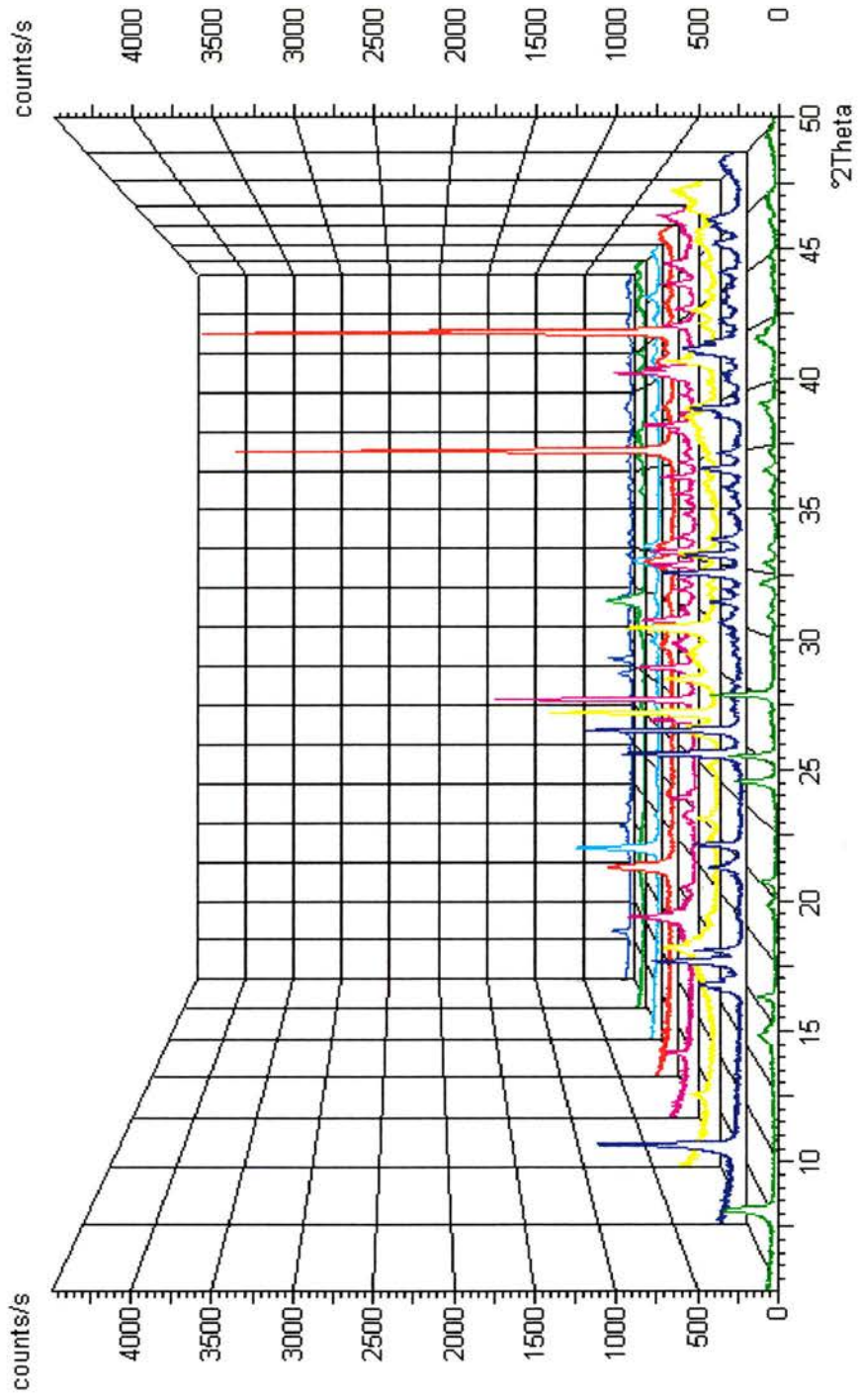


**Figure 3.13.** X-ray diffraction patterns of aluminoborate phases made in experiments 1 (back) to 8 (front). For experimental variables see Table 3.4.

## 3.5. Discussion

### 3.5.1. Boro-aluminophosphate Materials

The low boron levels in the crystalline solids indicates that the borate remains preferentially in solution. This behaviour explains the paucity of microporous borophosphates recorded in the literature, compared to the rich aluminophosphate chemistry.

The primary amines, as expected, act as efficient structure directing agents. Two known and two unknown phases were recorded. N-isopropylethylenediamine and N'-isopropyl-diethylenetriamine each produce apparently novel phases.

Isopropylamine is an interesting structure directing agent as by tuning synthesis conditions it can give a variety of phases. BAPO-14A, which was synthesised with this structure directing agent, had not previously been reported in the absence of fluoride ions although its structure was known.<sup>18</sup> By comparison with the powder X-ray pattern of the layered BAPO-*trans*-1,4-diaminocyclohexane material, phase  $\gamma$  appears to have a similarly layered structure. It is plausible to hypothesise two isopropylamine units arranged into a pseudo 1,4-diaminocyclohexane configuration.

### 3.5.2. Aluminoborate Materials

The statistical experimental design technique employed here proved very effective at allowing methodical investigation of the aluminoborate system considered. In the first set of experiments one composition stood out (due to the presence of a low angle XRD reflection) which readily enabled further synthesis to be carried out, centring on this point. During the second set of trials the optimum gel composition was refined, increasing the level of boron and calcium and reducing the level of aluminium in the preparation. The best gel composition was found to contain  $0.5\text{Al}_2\text{O}_3 : 9\text{B}_2\text{O}_3 : 2.8\text{CaO}$  rather than  $\text{Al}_2\text{O}_3 : 6\text{B}_2\text{O}_3 : 0.6\text{CaO}$  (which had produced an amorphous material during this study). The materials' powder X-ray diffraction patterns, while similar, are not the same which would suggest that the material reported in the literature is not itself phase pure.

### 3.6. Conclusions and Further Work

It was found that boron become included in the aluminophosphates only at very low levels but it is hypothesised, by analogy with materials previously examined in the laboratory, that the small percentage found will be in tetrahedral co-ordination in the as-prepared solids.

A statistically designed set of experiments with the *trans*-1,4-diaminocyclohexane template was successful in optimising the yield of product and in obtaining, through methodical variation of synthesis parameters, single crystals which enabled the phase to be identified as known. The low boron content indicated that these materials are of little commercial utility

Phase pure materials were synthesised with isopropylamine, one of which was found to be AlPO<sub>4</sub>-14A and the profile was Rietveld refined from synchrotron X-ray data.

Apparently novel materials were synthesised with the templates: N-isopropylethylenediamine and N'-isopropyldiethylenetriamine. Work must now be carried out to determine their structures.

Well crystalline aluminoborate phase (similar in X-ray profile to B-C7) was synthesised efficiently by the application of a qualitative set of statistically designed experiments. This material should now be characterised fully for applications in adsorption and catalysis.

### 3.7. References

1. R. H. Jones, J. M. Thomas, R. Xu, Q. Huo, A. K. Cheetham and A. V. Powell, *J. Chem. Soc., Chem. Commun.*, 1991, 1266.
2. W. Jianhua, F. Shouhua and X. Ruren, *J. Chem. Soc., Chem. Commun.*, 1989, 265.
3. A. F. Cronstedt, *Svenska Vetenskaps Akademiens Handlingar*, 1756, **17**, 120.
4. M. E. Davis and R. F. Lobo, *Chem. Mater.*, 1992, **4**, 756.
5. W. Loewenstein, *Am. Mineral.*, 1954, **39**, 92.
6. C. R. A. Catlow, A. R. George and C. M. Freeman, *J. Chem. Soc., Chem. Commun.*, 1996, 1311.

7. R. M. Barrer, *Hydrothermal Chemistry of Zeolites*, Academic Press, London, 1st edn., 1982, ch.1, pp. 8–20.
8. S. T. Wilson, B. M. Lok, C. A. Messina, T. R. Cannon and E. M. Flanigen, *J. Am. Chem. Soc.*, 1982, **104**, 1146.
9. *Atlas of Zeolite Structure Types*, eds. W. M. Meier, D. H. Olson and Ch. Baerlocher, Elsevier, London, 4th edn., 1996; R. Szostak, *Handbook of Molecular Sieves*, Van Nostrand Reinhold, New York, 1st edn., 1992.
10. E. M. Flanigen, R. L. Patton and S. T. Wilson, *Stud. Surf. Sci. Catal.*, 1988, **37**, 13.
11. S. Oliver, A. Kuperman, A. Lough and G. A. Ozin, *Chem. Mater.*, 1996, **8**, 2391; R. H. Jones, J. M. Thomas, R. Xu, Q. Huo, Y. Xu, A. K. Cheetham and D. Bieber, *J. Chem. Soc., Chem. Commun.*, 1990, 1170; W. Tieli, Y. Long and P. Wengin, *J. Solid State Chem.*, 1990, **89**, 392.
12. S. Oliver, A. Kuperman, A. Lough and G. A. Ozin, *J. Chem. Soc., Chem. Commun.*, 1996, 1761; D. A. Bruce, A. P. Wilkinson, M. G. White and J. A. Bertrand, *J. Chem. Soc., Chem. Commun.*, 1995, 2059.
13. S. Oliver, A. Kuperman, A. Lough and G. A. Ozin, *Inorg. Chem.*, 1996, **35**, 6373.
14. I. P. Appleyard, R. K. Harris and F. R. Fitch, *Zeolites*, 1986, **6**, 428.
15. R. Kniep, H. Günter, I. Boy and C. Röhr, *Angew. Chem. Int. Ed. Engl.*, 1997, **36**, 1013.
16. R. Kniep, G. Gozel, B. Eisenmann, C. Röhr, M. Asbrand and M. Kizilyalli, *Angew. Chem. Int. Ed. Engl.*, 1994, **33**, 749.
17. S. C. Sevov, *Angew. Chem. Int. Ed. Engl.*, 1996, **35**, 2630.
18. M. Goepper and J. L. Guth, *Zeolites*, 1991, **11**, 477.

## Chapter Four

# Boron Substituted Mullite Ceramics

### 4.1. Abstract

The effect of boron substitution on the crystallisation and structure of ceramic aluminosilicate mullite was examined for materials of varying composition within the  $\text{Al}_2\text{O}_3\text{-SiO}_2\text{-B}_2\text{O}_3$  system. A selection of phases were characterised by high resolution powder X-ray diffraction and MAS NMR spectroscopy.

Boron was found to accelerate crystallisation but may be partially lost at higher temperatures. Aluminoborate mullite was observed which broke down at higher temperatures to the phase  $9\text{Al}_2\text{O}_3\cdot 2\text{B}_2\text{O}_3$  and alumina. Boro-mullite was seen to crystallise over a wider range of compositions than previously reported and was phase pure by X-ray diffraction and NMR spectroscopy. Assuming the boron is present in the mullite structure, it is hypothesised that it is in a related trigonal site to that observed in  $9\text{Al}_2\text{O}_3\cdot 2\text{B}_2\text{O}_3$ , rather than in a tetrahedral site as was proposed before.

### 4.2. Introduction

Aluminosilicate mullite is a difficult structure because it is incommensurate; that is to say the lattice possesses long range order that has two or more periods, the ratio between them being an irrational number. This leads to a sinusoidal modulation of Al/Si order and oxygen vacancies that run through the structure on a larger scale than the unit cell. Before considering the structure it will be useful to examine the mineral sillimanite, which while structurally simpler, has many of the crystallographic features of mullite.

#### 4.2.1. The Structure of Sillimanite

Sillimanite is one of three naturally occurring polymorphs of  $\text{Al}_2\text{SiO}_5$ . Its structure consists of chains of edge-sharing  $\text{AlO}_6$ -octahedra running parallel to the *c*-axis.

These are cross-linked by double chains of aluminium and silicon containing tetrahedra that join to adjacent octahedra by corner-sharing (Figure 4.1.).

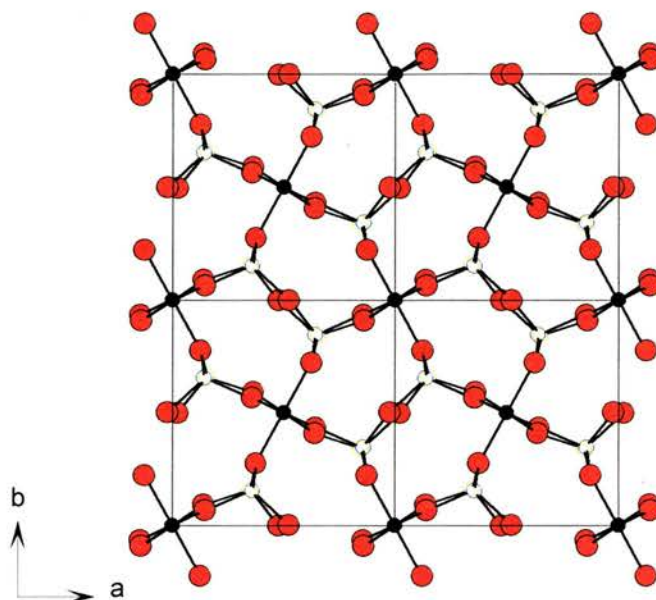


**Figure 4.1.** Sillimanite is composed of  $\text{AlO}_6$ -octahedra crosslinked by double chains of alternating aluminium and silicon containing tetrahedra.

The aluminium octahedra are elongated axially,  $30^\circ$  from the  $b$ -axis, towards the  $\text{O}_d$  oxygen. Within the double tetrahedral chains the cations are displaced towards the bridging  $\text{O}_c$  oxygen, creating a short bond.

Disorder of aluminium and silicon in the tetrahedral sites has been proposed, despite the charge imbalance between nearest neighbour tetrahedra and the fact that it would violate Loewenstein's rule which prohibits  $\text{Al-O-Al}$  units.<sup>1</sup> Single crystal refinements of sillimanite show no Si/Al disorder, but up to five percent disorder would be undetectable by this method.

Cameron *et al.*<sup>2</sup> used electron diffraction and infra red spectroscopy to look for silicon-aluminium disorder in fibrolite (an acicular form of sillimanite). They proposed that in a disordered system the space group would change from  $Pbnm$  to  $Pbam$ , and that consequently the intensity of  $l$ -odd reflections would diminish, so that in a completely disordered system they would be zero. Their data showed

fibrolite to be in the *Pbnm* (ordered) space group. Yet Sahl *et al.*<sup>3</sup> disagreed, maintaining that complete disorder would preserve the *l*-odd reflections.

Solid state NMR has been applied to this problem; silicon was chosen because it has none of the quadrupolar interactions of the aluminium nucleus. The <sup>29</sup>Si MAS NMR spectra shows a small amount of disorder of around one to two percent.<sup>4</sup>

There is evidence for the existence of a solid solution between sillimanite and mullite. Burnham<sup>5</sup> concluded, after examining the structures, that there should be no reason why there cannot be a full solid solution between the two. The *mullitization* of sillimanite was examined by Guse *et al.*<sup>6</sup> who observed, from X-ray analysis, a topotactic sillimanite to mullite reaction occurring in a sample heated at 1600 °C (1 atm.) for 25 – 30 hours.

#### 4.2.2. Aluminosilicate Mullite

The mullite structure is observed in materials with compositions between sillimanite ( $\text{Al}_2\text{SiO}_5$ ) and alumina ( $\text{Al}_2\text{O}_3$ ) of general form  $\text{Al}_2[\text{Al}_{2+2x}\text{Si}_{2-2x}]\text{O}_{10-x}$ . Mullite with  $x = 0.25$  (3/2 mullite,  $3\text{Al}_2\text{O}_3 \cdot 2\text{SiO}_2$ ) and 0.40 (2/1 mullite,  $2\text{Al}_2\text{O}_3 \cdot \text{SiO}_2$ ) have been described as the main constituents of sinter-mullite and fused-mullite respectively. Siliceous ( $x < 0.20$ ) and aluminium-rich<sup>7</sup> ( $x > 0.60$ ) are also possible. Cameron *et al.*<sup>8</sup> have found the unit cell dimensions, *a* and *b*, vary almost linearly with *x* (i.e. alumina content). The *a*-axis is slightly smaller and increases while *b* decreases (Figure 4.2.). Ban *et al.*<sup>9</sup> applied this correlation to determine the composition of unknown mullites.

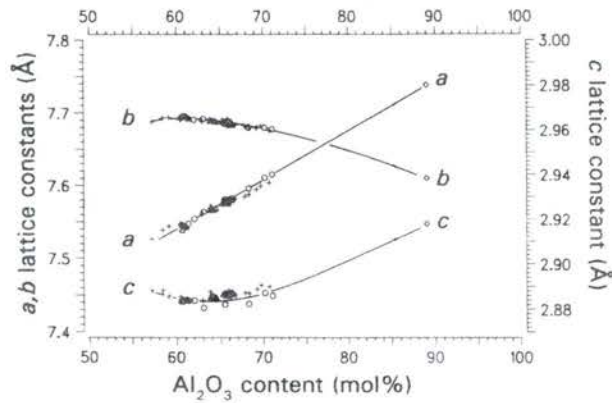


**Figure 4.2.** The relationship between lattice parameters and aluminium content. Data collated by Fisher *et al.*: triangles,<sup>10</sup> crosses,<sup>11</sup> open circles,<sup>9</sup> lozenges.<sup>7</sup>

The composition where  $a = b$  is called *tetragonal* mullite, or more correctly *pseudotetragonal metric*<sup>12</sup> since the symmetry of the crystal structure remains orthorhombic.

The structure of mullite can be extrapolated from that of sillimanite by imagining aluminium substituted for silicon,  $2\text{Si}^{4+} + \text{O}^{2-} \rightarrow 2\text{Al}^{3+} + \diamond$ , with resulting oxygen vacancies ( $\diamond$ ). These vacancies create an incommensurate modulation that is periodic in the structure, but on a larger scale than the unit cell. As silicon is exchanged for aluminium the position and occupancy of the tetrahedral cation sites, and some oxygen sites, changes (Figure 4.3.).

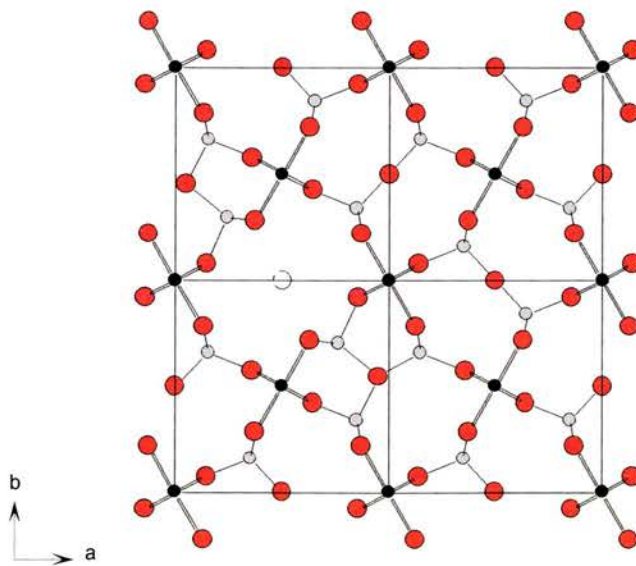


**Figure 4.3.** As sillimanite, mullite is composed of  $\text{AlO}_6$ -octahedra crosslinked by chains of tetrahedral aluminium and silicon. Vacancies in these tetrahedra, due to the need for charge balance after the substitution of silicon by aluminium, create an incommensurate modulation and displaced the tetrahedral cation sites (T) to a new site ( $\text{T}^*$ ).

In mullite, as sillimanite, there are edge-sharing chains of octahedrally co-ordinated aluminium atoms running parallel to the  $c$ -axis, two per unit cell. These are cross-linked by aluminium and silicon tetrahedra (four per unit cell), arranged in double-chains, and linked through the  $\text{O}_c$  oxygen. It is this oxygen that is lost when extra aluminium is included in the structure. The adjacent tetrahedral cation sites (T) become three co-ordinate to oxygen and displace to a new  $\text{T}^*$  site to bond with an adjacent  $\text{O}_c$  site. A new three co-ordinate oxygen is formed that displaces from the symmetry centre, towards the  $\text{T}^*$  site, to a new position,  $\text{O}_c^*$ .

The site occupancies are related to the compositional variable  $x$ , which is effectively the stoichiometric number of oxygen vacancies. Angel *et al.*<sup>13</sup> related it to the site occupancy in aluminosilicate mullite, thus:

$$\begin{array}{ll} \text{O on } \text{O}_c: & 1 - \frac{3}{2}x & \text{Si (T plus } \text{T}^*): & \frac{1}{2} - \frac{1}{2}x \\ \text{O on } \text{O}_c^*: & \frac{1}{2}x & \text{Al (T plus } \text{T}^*): & \frac{1}{2} + \frac{1}{2}x \end{array}$$

The total number of atoms on the T site is  $1 - x/2$  while the other  $x/2$  is on  $\text{T}^*$  (half the number of oxygen vacancies since the other half has been displaced into the adjacent unit cell). Now consider the oxygen occupancies on  $\text{O}_c$  and  $\text{O}_c^*$ : the total amount must be  $1 - x/2$  as  $\text{O}_c$  is on a special equivalent position of multiplicity two and  $\text{O}_c^*$  is on a position of multiplicity four. The occupancy of  $\text{O}_c^*$  can be correlated to  $\text{T}^*$  so that each  $\text{O}_c^*$  site is occupied by  $x$  oxygen. By subtraction we have  $1 - 3/2x$  oxygen on  $\text{O}_c$ . It should be noted that if  $x$  is 0.67 then the  $\text{O}_c$  site would be completely vacant and, as more aluminium was included in the structure, oxygen should have to be removed from elsewhere.

The  $\text{T}^*$  site contains mostly aluminium, but may contain some silicon. Angel *et al.* conducted a refinement of powder X-ray diffraction data but failed to resolve the

question of silicon-aluminium occupancy on this site. Previous studies by Sadanaga *et al.*<sup>14</sup> considered the site to be exclusively populated by aluminium, in contrast to Durovic *et al.*<sup>15</sup> and Burnham<sup>16</sup> who thought that a small amount of silicon was present. These results were all based on the observation that the anisotropic temperature factors obtained for the  $O_{ab}$  and  $O_d$  oxygens that co-ordinate the T and  $T^*$  sites were very large. Angel *et al.* refined the occupancies of the T and  $T^*$  sites which showed that the ratio of aluminium-to-silicon was the same (2 : 1). This was inconclusive not only because of the two elements similar scattering factors but also because of the positions' fractional occupancy. An examination of the tetrahedral bond distances was then carried out. Oxygen can be seen to move towards sites rich in silicon and away from those high in aluminium, while the cations' position does not change. Bond lengths to T and  $T^*$  were calculated from the oxygen positions  $O_{ab}$  and  $O_d$  (derived from Fourier skew maps) but these did not support the refined occupancies. Instead they indicated that either very little or no silicon resides in the  $T^*$  site.

Solid state NMR has allowed a distinction to be made between the two triclusters previously denoted  $T^*$  based on X-ray diffraction, one is denoted  $T'$  and the other  $T^*$ . Kunath-Fundrei *et al.*<sup>17</sup> used the improved resolution of the  $^{27}\text{Al}$  MAS sidebands of the inner satellite transition to assign the chemical shifts  $\delta_{\text{Al}}$  68 (T), 53 ( $T'$ ) and 45 ( $T^*$ ).

#### 4.2.3. Boron Substitution in Mullite

The phase diagram  $\text{Al}_2\text{O}_3\text{-SiO}_2\text{-B}_2\text{O}_3$  (Figure 4.4.) has been investigated revealing an area in which boro-aluminosilicate mullite can be synthesised.

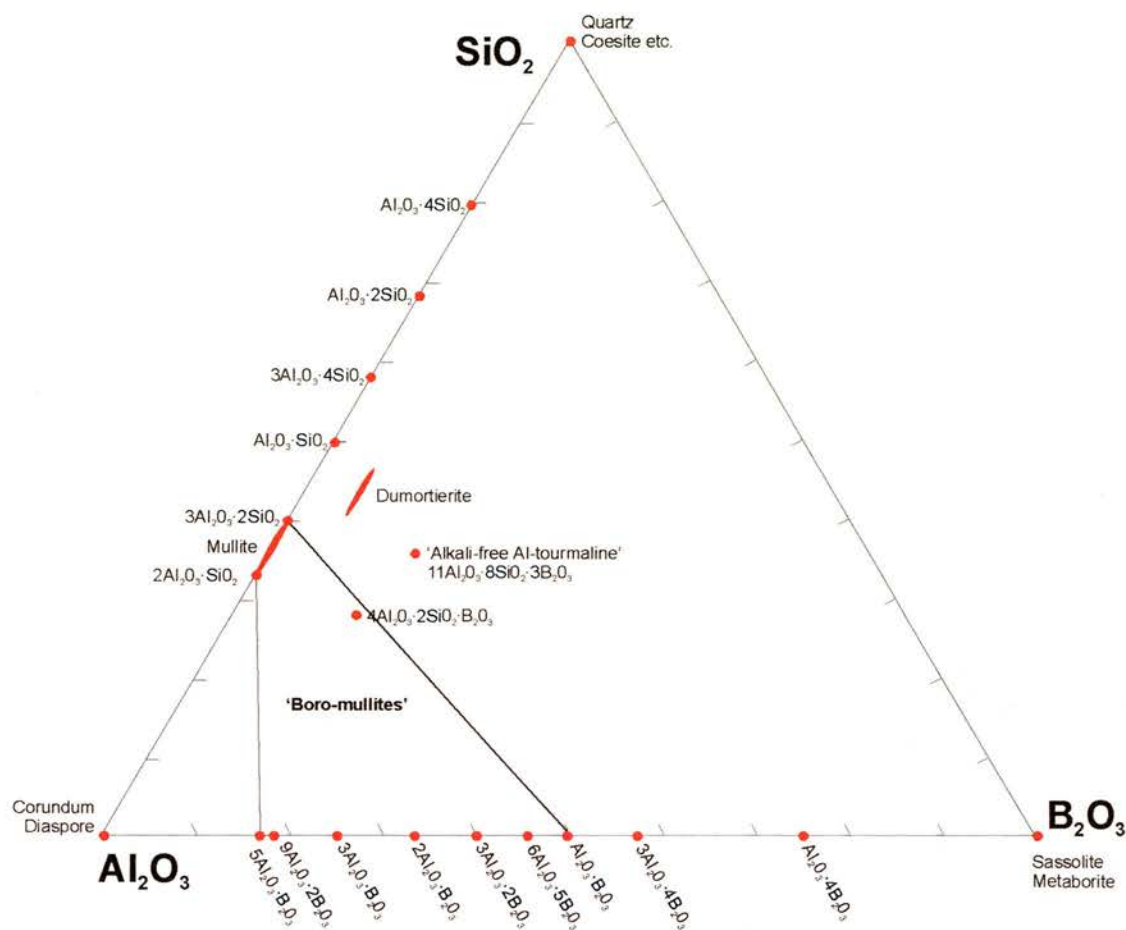


**Figure 4.4.** The  $\text{Al}_2\text{O}_3$ – $\text{SiO}_2$ – $\text{B}_2\text{O}_3$  phase diagram showing the proposed boro-mullite region.<sup>18</sup>

Mazza *et al.*<sup>19</sup> synthesised materials in the  $\text{Al}_2\text{O}_3$ – $\text{B}_2\text{O}_3$  phase diagram with mullite-type XRD patterns of composition 15 – 50 mol%  $\text{B}_2\text{O}_3$ . The materials:  $\text{Al}_5\text{BO}_9$  and  $\text{Al}_4\text{B}_2\text{O}_9$  have pseudotetragonal unit cells ( $a = b$ ,  $Pbam$ ). After heating at 900 – 1000 °C these materials evolve to  $9\text{Al}_2\text{O}_3 \cdot 2\text{B}_2\text{O}_3$  and  $2\text{Al}_2\text{O}_3 \cdot \text{B}_2\text{O}_3$  by, they proposed, the progressive ordering of oxygen vacancies.

The phase  $9\text{Al}_2\text{O}_3 \cdot 2\text{B}_2\text{O}_3$  had previously been observed by Dietzel *et al.*<sup>20</sup> who recognised the solid solution between the aluminosilicate and aluminoborate mullites. Single crystal X-ray diffraction yielded the structure to Ihara *et al.*,<sup>21</sup> it is again characterised by infinite chains of  $\text{AlO}_6$ -octahedra, running parallel to the  $c$ -axis. The length of this axis is similar to that of sillimanite, indicating order within the units that link the chains. The  $b$ -axis has doubled, relative to sillimanite (and mullite) because the structure contains two different units, arranged in the same way

as the  $\text{AlO}_6$ -octahedra, but with cations Al(2), Al(3), Al(4) and B at different heights in the framework (Figures 4.5. and 4.6.).

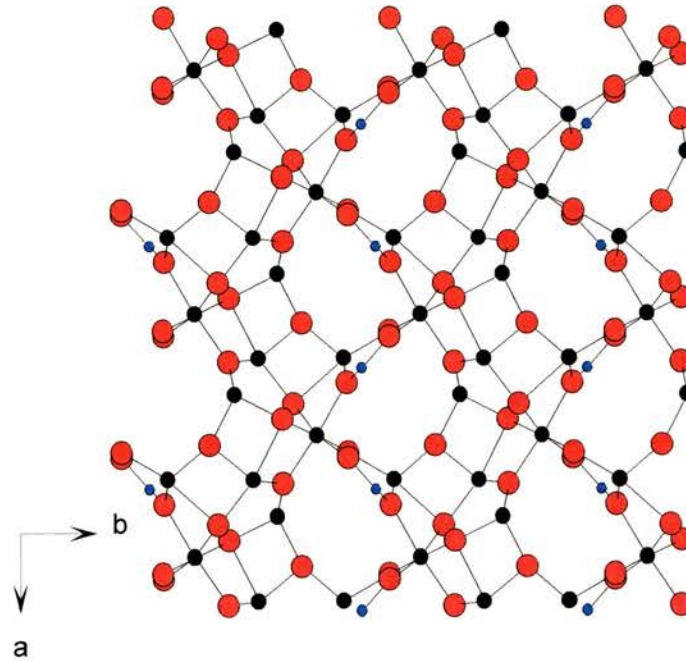


**Figure 4.5.** Structure of the phase  $9\text{Al}_2\text{O}_3 \cdot 2\text{B}_2\text{O}_3$  shows similarities to sillimanite and mullite in the  $\text{AlO}_6$  chains but differs in the way they are linked.

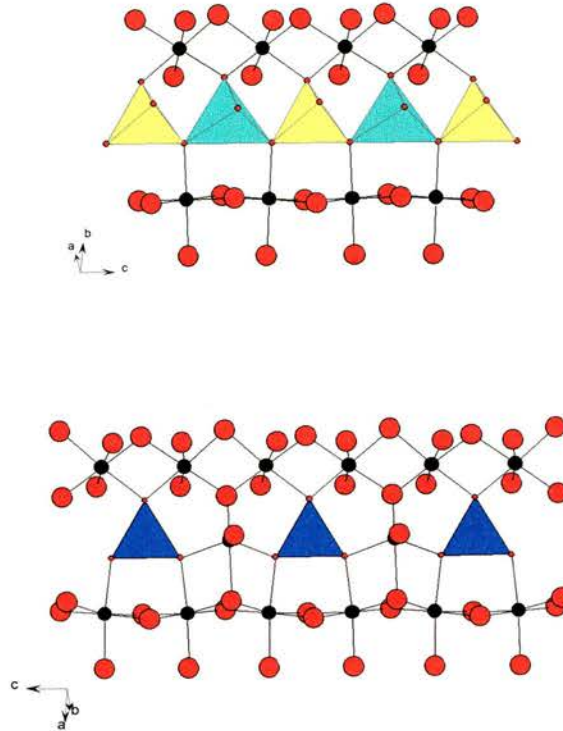


**Figure 4.6.** Comparison of the way the parallel chains of AlO<sub>6</sub> octahedra are linked via tetrahedra in sillimanite (above) and trigonal BO<sub>3</sub> and tetrahedra AlO<sub>4</sub> in 9Al<sub>2</sub>O<sub>3</sub>·2B<sub>2</sub>O<sub>3</sub> (below).

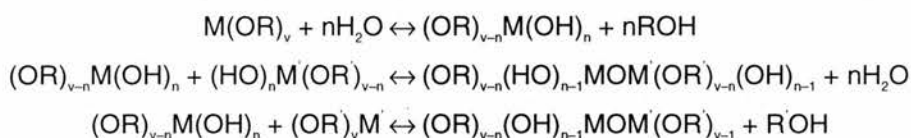
### 4.3. Experimental

#### 4.3.1. Synthesis

Several methods of synthesis have been reported in the literature for the mullite phase. These include sol-gel techniques and melt crystallisation.<sup>22</sup> The materials made for study here were synthesised by the sol-gel method. The sol, a colloidal suspension of particles in a solvent, was hydrolysed to form a gel, a semi-rigid solid with solvent contained within an amorphous framework. On calcination the final product formed. The principal advantage of this procedure are the homogeneity of product that may be obtained and the relatively low temperatures at which crystalline phases may be produced. Heating removes the solvent as well as decomposing the alkoxide anions to oxide, while allowing rearrangements of the structure and crystallisation to take place.

The choice of aluminium, silicon and boron sources is governed by the need to have approximately equal hydrolysis rates of each constituent to guarantee a

homogeneous gel. In sol-gel syntheses this has meant using colloidal or alkoxide based preparations. The rate of hydrolysis of silicon alkoxides is slow compared to other metal alkoxides, but several methods have been proposed to reduce the difference: pre-hydrolysis of the silicon alkoxide, using aluminium nitrate, or both, using silicon aluminium ester as precursor, or reducing the rate of aluminium hydrolysis with linear, low weight, alkoxy groups. The hydrolysis reactions operating within the gelation process may include the following:



where R = organic; M = metal of group 3 or 4; V = the valency of the metal.

Alternatively the synthesis can be carried out without water and so circumvent the previously derived equations.

An aqueous alkoxide-based system was chosen for the preparations described here. The boro-mullite sol was formed by the sequential addition of aluminium tri-sec-butoxide (97 %, Aldrich), tetraethyl orthosilicate (98 %, Aldrich) and tributylborate (99 %, Aldrich) to propan-2-ol (99.5 %, Fisher), with stirring. All materials were used without further purification. Aqueous hydrochloric acid (36.86 %, Fisher) was then added and the covered mixture left to gel overnight. Low heating (400 °C) initially under nitrogen, to evaporate the solvent, then oxygen to oxidise the organic materials, was carried out before the gel was divided and each portion calcination at a temperature typically between 900 – 1200 °C upon which the crystalline product formed.

### 4.3.2. Crystallography

Routine characterisation of the materials produced was carried out on one of two Philips X'Pert System powder X-ray diffractometers, in reflectance mode (Bragg-Bentano geometry), using Cu K $\alpha$  radiation ( $\lambda = 1.542 \text{ \AA}$ ) with secondary monochromation and a scintillation counter. Powder samples were placed on an aluminium plate sample holder and data collected in 45 minutes over the  $2\theta$  range 10 – 50°, with a 0.02° step.

High quality data was obtained on a Stoe STADI P high resolution powder X-ray diffractometer in transmission mode (Debye-Scherrer geometry), using primary monochromated Cu  $K_{\alpha_1}$  radiation ( $\lambda = 1.54056 \text{ \AA}$ ) and a linear position-sensitive detector covering  $7^\circ$  in  $2\theta$ . Samples were typically mounted in 0.7 mm quartz capillaries and data collected in 14 hours over the  $2\theta$  range  $10 - 85^\circ$  and with a step size of  $0.02^\circ$ . This instrument was also used to collect variable temperature data using a furnace attachment capable of holding 0.5 mm quartz capillaries.

Rietveld refinement was carried out on data collected with the Stoe STADI P diffractometer using the General Structure Analysis System<sup>23</sup> (GSAS) suite of programs running under MS-DOS.

### 4.3.3. MAS NMR Spectroscopy

Data were collected at the EPSRC Solid State NMR Facility in Durham on a Varian UNITY plus 300 spectrometer using a Doty Scientific MAS probe with 7 mm o.d. rotors (of zirconia) for  $^{29}\text{Si}$  spectra and a Doty MAS probe with 5 mm o.d. rotors (of silicon nitride) for  $^{27}\text{Al}$  and  $^{11}\text{B}$  spectra. External shift reference samples were used:  $\text{BF}_3/\text{OEt}_2$ ,  $\text{AlCl}_3$  and  $(\text{CH}_3)_4\text{Si}$  for the  $^{11}\text{B}$ ,  $^{27}\text{Al}$  and  $^{29}\text{Si}$  spectra respectively.

## 4.4. Results

Materials were prepared in compositions given in the  $\text{Al}_2\text{O}_3\text{-SiO}_2\text{-B}_2\text{O}_3$  triangular diagram (Figure 4.7.), and those compositions that gave mullite that was phase pure by XRD (see later) are indicated. The compositions  $2\text{Al}_2\text{O}_3\cdot\text{SiO}_2$ ,  $3\text{Al}_2\text{O}_3\cdot 2\text{SiO}_2$ ,  $5\text{Al}_2\text{O}_3\cdot\text{B}_2\text{O}_3$  and  $\text{Al}_2\text{O}_3\cdot\text{B}_2\text{O}_3$  represent the extremes of composition between which boro-mullite is reported to crystallise in the literature. In this study mullite was synthesised outside this region at  $1000^\circ\text{C}$  and  $1200^\circ\text{C}$  at compositions of  $6.5\text{Al}_2\text{O}_3\cdot 5\text{SiO}_2\cdot\text{B}_2\text{O}_3$  and  $6\text{Al}_2\text{O}_3\cdot 5\text{SiO}_2\cdot 1.5\text{B}_2\text{O}_3$  (very close to the composition of dumortierite:  $\text{Al}_{7-x}(\text{BO}_3)[\text{Al}_y\text{Si}_{3-y}\text{O}_{15-3x-y}(\text{OH})_{3x+y}]$  where  $x > 0.1$  and  $y < 0.5$ , which is reported in other studies). Boro-mullite is known to be a breakdown product of dumortierite at low pressures, but here dumortierite was not found. Mullite formed in the presence of boron after less than three hours heating at  $1000^\circ\text{C}$ ; crystallinity improved with further heating.

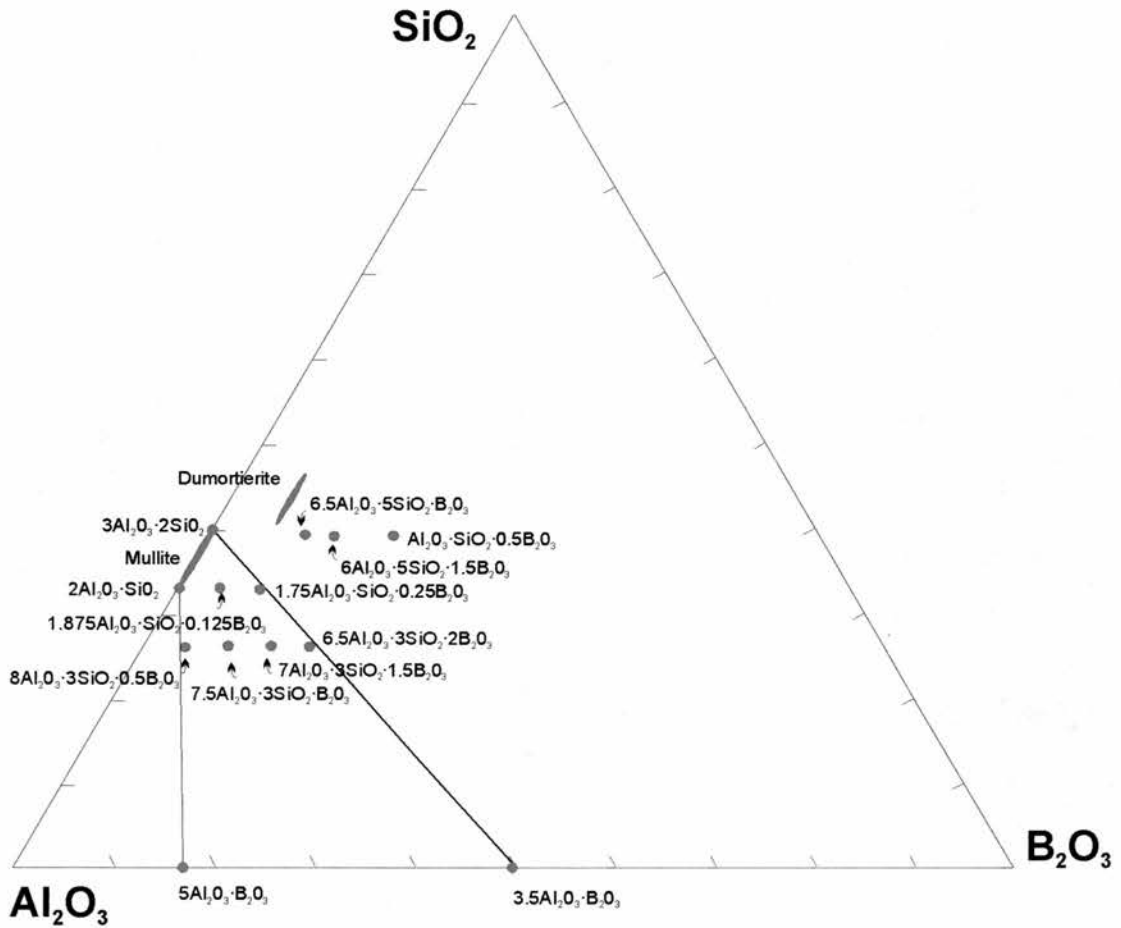


**Figure 4.7.** The  $\text{Al}_2\text{O}_3$ - $\text{SiO}_2$ - $\text{B}_2\text{O}_3$  triangular composition diagram shown in Figure 4.4. showing the materials' compositions examined during this study. As described in more detail later, all compositions except those without boron gave mullite related phases after heating at  $1000^\circ\text{C}$ , and the aluminoborate compositions gave mullite related phases at  $1000^\circ\text{C}$  and broke-down to give  $9\text{Al}_2\text{O}_3 \cdot 2\text{B}_2\text{O}_3$  at higher temperatures.

### 4.4.1. Aluminoborate Phases

#### 4.4.1.1. XRD Results

At temperatures below 1100–1200 °C it appears that aluminoborate mullite is formed over the range of compositions studied (see XRD patterns for heating products of material with starting composition  $5\text{Al}_2\text{O}_3\cdot\text{B}_2\text{O}_3$ , Figure 4.8., for example). The sharp reflections in these patterns correspond to those observed for aluminosilicate mullite—see section 4.4.2. Extra broad reflections were observed suggesting poorly ordered domains with a structure related to the  $9\text{Al}_2\text{O}_3\cdot 2\text{B}_2\text{O}_3$  phase.

At temperatures of *ca.* 1100 °C the aluminoborate mullite-related phase converts to the  $9\text{Al}_2\text{O}_3\cdot 2\text{B}_2\text{O}_3$  phase (plus alumina in the case of the more alumina rich precursor). This was confirmed as the observed phase by a Rietveld refinement of the sample prepared from heating an original composition of  $\text{Al}_2\text{O}_3\cdot\text{B}_2\text{O}_3$ .

The  $9\text{Al}_2\text{O}_3\cdot 2\text{B}_2\text{O}_3$  phase produced was Rietveld refined from the starting model proposed by Garche *et al.*<sup>27</sup> to give  $R_p = 4.94\%$ ,  $R_{wp} = 6.42\%$ . The Rietveld plot is shown in Figure 4.10., indicating the model was very good and that the  $9\text{Al}_2\text{O}_3\cdot 2\text{B}_2\text{O}_3$  phase was synthesised. Table 4.1. show the refined lattice parameters, atomic co-ordinates and temperature factors, while Table 4.2. shows selected bond lengths and angles.

Name	X	Y	Z	$U_{iso} (\text{Å}^2)$
B	0.707(5)	0.0269(22)	0.000000	0.025
Al1	0.5032(11)	0.3831(6)	0.2522(14)	0.025
Al2	0.6817(14)	0.2431(6)	0.500000	0.025
Al3	0.6900(21)	0.0538(5)	0.500000	0.025
Al4	0.8330(12)	0.2958(6)	0.000000	0.025
O1	0.7894(13)	0.0478(10)	0.2161(17)	0.025
O2	0.7071(13)	0.3092(9)	0.2359(23)	0.025
O3	0.5284(22)	0.1422(15)	0.500000	0.025
O4	0.9276(19)	0.1927(13)	0.000000	0.025
O5	0.8736(23)	0.1743(11)	0.500000	0.025
O6	0.5803(21)	0.4492(13)	0.000000	0.025
O7	0.5930(20)	0.4540(12)	0.500000	0.025
a = 7.6777(2) Å, b = 14.9828(5) Å, c = 5.65642(14) Å				
vol. = 650.68 Å <sup>3</sup>				

**Table 4.1.** Atomic co-ordinates of the  $9\text{Al}_2\text{O}_3\cdot 2\text{B}_2\text{O}_3$  phase, refined in *A2,am*.

<b>BO<sub>3</sub>-triangle</b>		
B – O(1)	×2	1.413(24)
B – O(7)		1.40(4)
mean		1.409
O(1) – B – O1		119.9(32)
O(1) – B – O7		116.7(16)
<b>Al(1)–O<sub>6</sub>-octahedron</b>		
Al(1) – O(1)		1.949(12)
Al(1) – O(2)		1.920(13)
Al(1) – O(4)		1.895(15)
Al(1) – O(5)		1.940(14)
Al(1) – O(6)		1.835(15)
Al(1) – O(7)		1.890(14)
mean		1.905
<b>Al(2)–O<sub>5</sub>-polyhedron</b>		
Al(2) – O(2)	×2	1.804(12)
Al(2) – O(3)		1.916(19)
Al(2) – O(4)		2.176(20)
Al(2) – O(5)		1.798(21)
mean		1.900
<b>Al(3)–O<sub>5</sub>-polyhedron</b>		
Al(3) – O(1)	×2	1.779(12)
Al(3) – O(3)		1.817(23)
Al(3) – O(5)		2.291(19)
Al(3) – O(6)		1.780(18)
mean		1.889
<b>Al(4)–O<sub>4</sub>-polyhedron</b>		
Al(4) – O(2)	×2	1.659(14)
Al(4) – O(3)		1.765(21)
Al(4) – O(4)		1.705(21)
mean		1.697

**Table 4.2.** Selected bond lengths (Å) and angles (°) of the 9Al<sub>2</sub>O<sub>3</sub>·2B<sub>2</sub>O<sub>3</sub> phase.

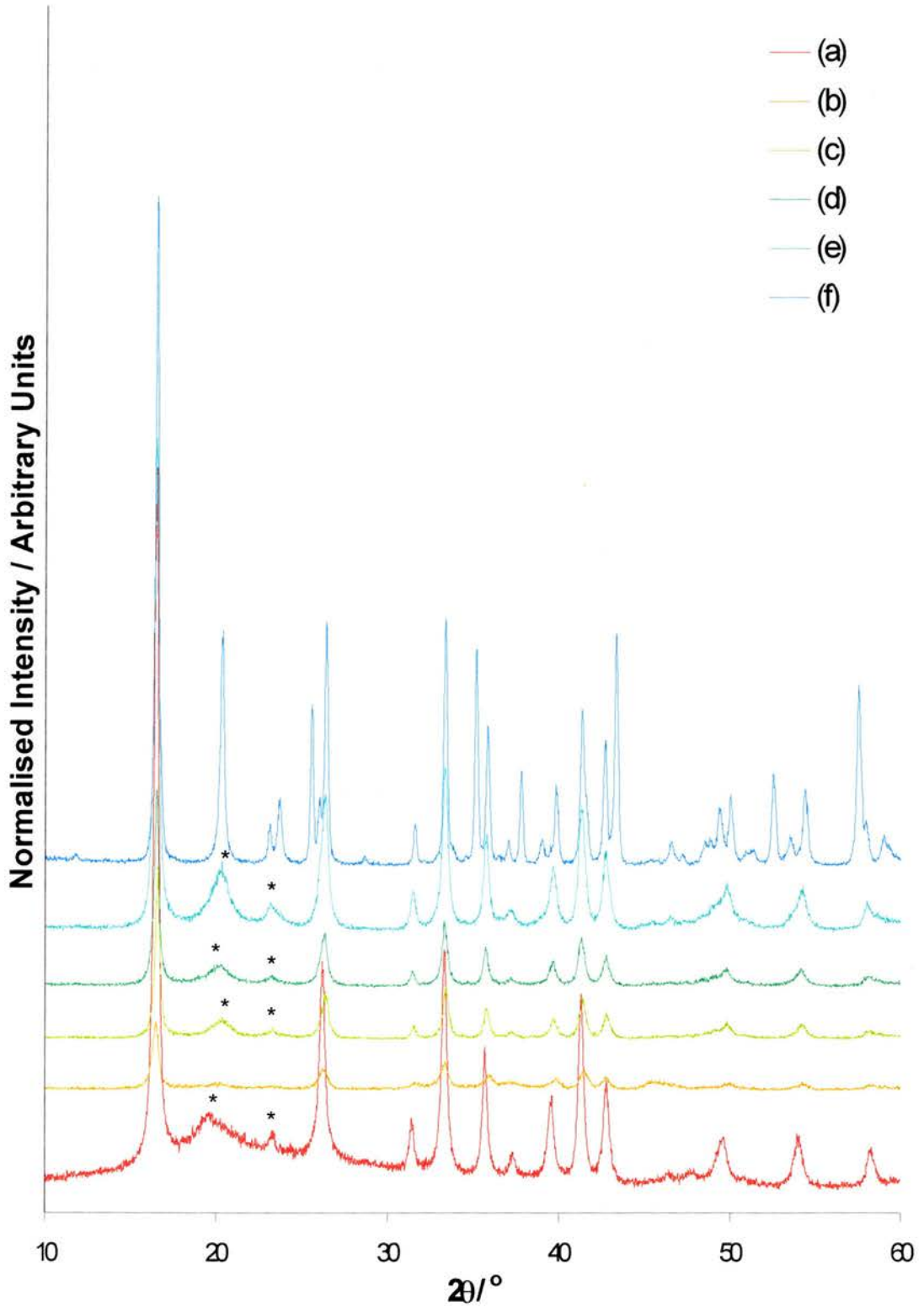


**Figure 4.8.** X-ray diffraction patterns collected from a sample of initial composition:  $5\text{Al}_2\text{O}_3 \cdot \text{B}_2\text{O}_3$  crystallised in 12 hours at (a) 900 °C (b) 1000 °C (c) 1050 °C (d) 1100 °C (e) 1150 °C (f) 1200 °C. (\*) indicates non-mullite reflections in the diffraction patterns.

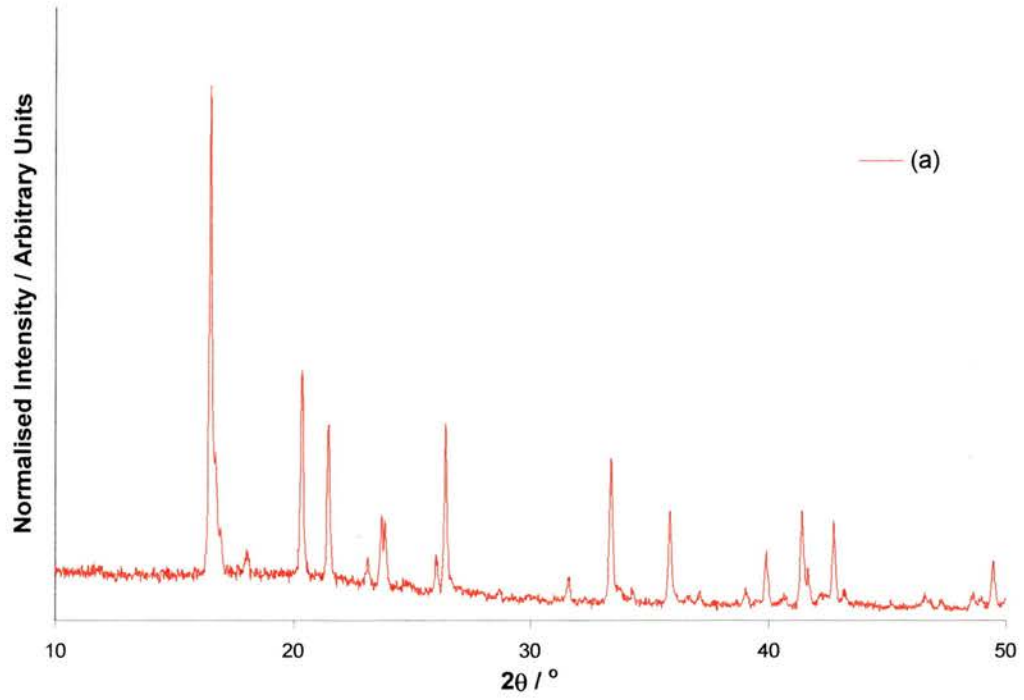


**Figure 4.9.** (a) X-ray diffraction pattern collected from a sample of initial composition:  $\text{Al}_2\text{O}_3\cdot\text{B}_2\text{O}_3$  crystallised in 24 hours at 1100 °C.

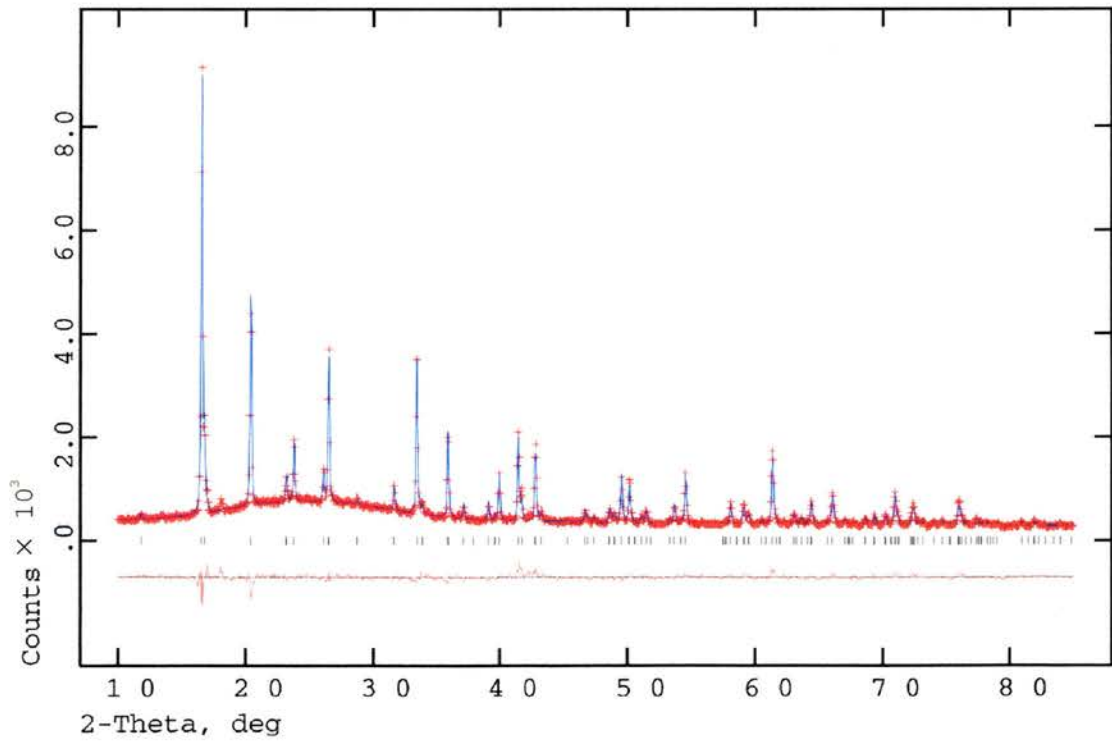


**Figure 4.10.** Rietveld refinement plot of  $9\text{Al}_2\text{O}_3\cdot 2\text{B}_2\text{O}_3$  showing simulated pattern (blue line), experimental profile (red crosses) and difference plot (red line).

#### 4.4.1.2. NMR Results

$^{27}\text{Al}$  and  $^{11}\text{B}$  MAS NMR were carried out on the aluminoborate species formed by heating starting compositions  $\text{Al}_2\text{O}_3\cdot\text{B}_2\text{O}_3$  (at 1100 °C) and  $5\text{Al}_2\text{O}_3\cdot\text{B}_2\text{O}_3$  (at 900 °C and 1200 °C). As described previously the former is phase pure  $9\text{Al}_2\text{O}_3\cdot 2\text{B}_2\text{O}_3$  by XRD, indicating appreciable boron loss, and the latter is a mixture of this phase and  $\alpha$ -alumina.

$^{11}\text{B}$  NMR of oxide systems is characterised by boron in trigonal and tetrahedral geometries. Whilst tetrahedral boron is spherically symmetrical, and gives rise to a single sharp resonance, trigonal boron gives a characteristic ‘horn’ lineshape due to quadrupolar interactions.

As expected from the crystal structure, the sample that refines as the 9 : 2 phase has boron in trigonal geometry (with a quadrupole coupling constant of 2.64 MHz, asymmetry of 0.13 and an isotopic shift of  $\delta_{\text{B}}$  17.6). A small amount (*ca.* 2 %) of a second species with shift  $\delta_{\text{B}}$  -1.3 is also present (Figure 4.11.).

The bandshape observed in the other materials’ ( $5\text{Al}_2\text{O}_3\cdot\text{B}_2\text{O}_3$ )  $^{11}\text{B}$  spectra is also very similar after heating at both 900 and 1200 °C and is again typical for three-coordinate species with axial symmetry. Simulations of the spectra of the 900 °C heated sample give a quadrupole coupling constant of 2.63 MHz, asymmetry of 0 and isotropic shift of  $\delta_{\text{B}}$  17.5 for the trigonal boron and show that a further 1 % boron takes up four-coordinate geometry. Simulations without this site do not fit the data accurately. At higher crystallisation temperatures more four-coordinate species are observed.

The aluminium spectrum of the material  $5\text{Al}_2\text{O}_3\cdot\text{B}_2\text{O}_3$  crystallised at 900 °C shows the typical mullite pattern of octahedral and tetrahedral sites. The spectrum becomes more complicated on heating at 1200 °C, consistent with the change of phase to  $9\text{Al}_2\text{O}_3\cdot 2\text{B}_2\text{O}_3$ . The spectrum of the  $\text{Al}_2\text{O}_3\cdot\text{B}_2\text{O}_3$  sample heated at 1100 °C also shows a complex  $^{11}\text{Al}$  spectrum, which is taken to be characteristic of the 9 : 2 phase.

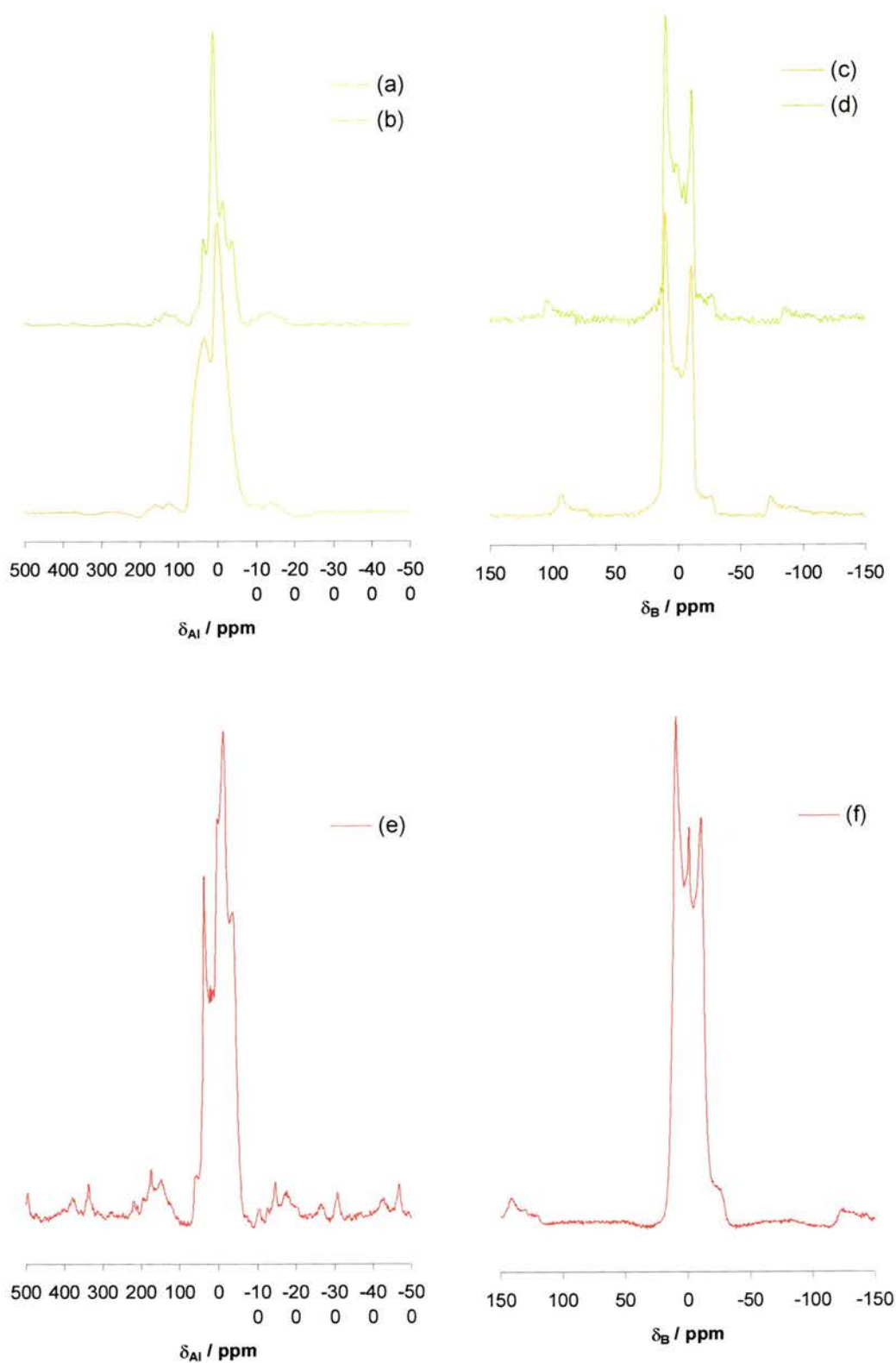


**Figure 4.11.** MAS NMR of aluminoborate phase  $5\text{Al}_2\text{O}_3 \cdot \text{B}_2\text{O}_3$  900 °C (a)  $^{27}\text{Al}$ , (c)  $^{11}\text{B}$ , 1200 °C (b)  $^{27}\text{Al}$ , (d)  $^{11}\text{B}$ ; and  $\text{Al}_2\text{O}_3 \cdot \text{B}_2\text{O}_3$  1100 °C (e)  $^{27}\text{Al}$ , (f)  $^{11}\text{B}$ .

## 4.4.2. Boro-aluminosilicate Phases

### 4.4.2.1. XRD Results

Powder X-ray diffraction was performed to determine the nature of the phases produced during synthesis and to check whether the crystalline samples were monophasic. Figure 4.12. shows a series of eight materials (crystallised at 1000 °C) from within the  $\text{Al}_2\text{O}_3\text{-SiO}_2\text{-B}_2\text{O}_3$  composition diagram; boron content of the starting gel influences crystallinity as can be seen from the fact that the materials containing boron are much more crystalline than those that do not.

The most highly crystalline materials were formed around the composition:  $1.875\text{Al}_2\text{O}_3\cdot\text{SiO}_2\cdot 0.125\text{B}_2\text{O}_3$ . Crystallinity was achieved at a final temperature of 1000 °C but improved slightly on going to 1200 °C. Further structural analysis was carried out on these materials. Even after 12 hours at 1200 °C aluminosilicate of compositions  $3\text{Al}_2\text{O}_3\cdot 2\text{SiO}_2$  and  $2\text{Al}_2\text{O}_3\cdot\text{SiO}_2$  were amorphous, indicating the major effect boron has in accelerating crystallisation.

Subtle effects may be illustrated by comparing Figure 4.12 (c) with (e) and (d) with (f) where each pair differs in aluminium-to-silicon ratio but has a constant amount of boron: similar levels of crystallinity are observed in the diffraction patterns. Yet if silicon content is held constant, as in (b), (c), (d) crystallinity reaches a maximum before falling slightly; this is also observed by comparison of (a), (c) and (f) where aluminium is constant.

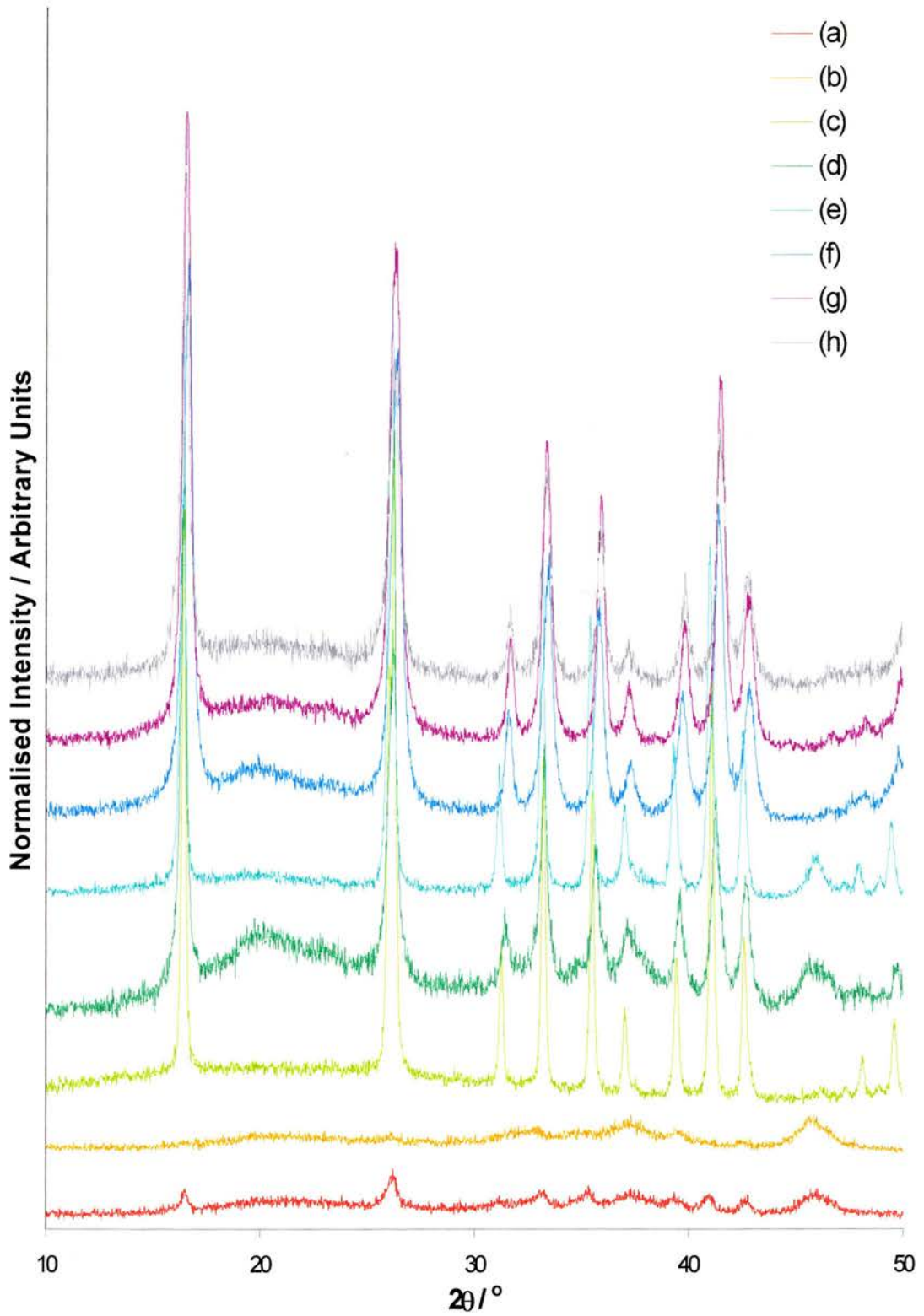


**Figure 4.12.** X-ray diffraction patterns collected from samples crystallised in 12 hours at 1000 °C from initial composition (a)  $3\text{Al}_2\text{O}_3 \cdot 2\text{SiO}_2$  (b)  $2\text{Al}_2\text{O}_3 \cdot \text{SiO}_2$  (c)  $1.875\text{Al}_2\text{O}_3 \cdot \text{SiO}_2 \cdot 0.125\text{B}_2\text{O}_3$  (d)  $1.75\text{Al}_2\text{O}_3 \cdot \text{SiO}_2 \cdot 0.25\text{B}_2\text{O}_3$  (e)  $8\text{Al}_2\text{O}_3 \cdot 3\text{SiO}_2 \cdot 0.5\text{B}_2\text{O}_3$  (f)  $7.5\text{Al}_2\text{O}_3 \cdot 3\text{SiO}_2 \cdot \text{B}_2\text{O}_3$  (g)  $7\text{Al}_2\text{O}_3 \cdot 3\text{SiO}_2 \cdot 1.5\text{B}_2\text{O}_3$  (h)  $6.5\text{Al}_2\text{O}_3 \cdot 3\text{SiO}_2 \cdot 2\text{B}_2\text{O}_3$ .

Heating at 1200 °C improves crystallinity only slightly. This is observed in the case of the material of initial gel composition  $1.875\text{Al}_2\text{O}_3 \cdot \text{SiO}_2 \cdot 0.125\text{B}_2\text{O}_3$  (Figure 4.13.) which has been heated at increasing increments of 50 degrees from 1000 °C – 1200 °C. Figures 4.14. and 4.15. show materials of composition  $6.5\text{Al}_2\text{O}_3 \cdot 5\text{SiO}_2 \cdot \text{B}_2\text{O}_3$  being heated at progressively higher temperatures and for increasingly longer times, respectively. The materials formed are mullite-like, yet form outside the region originally proposed for these materials.

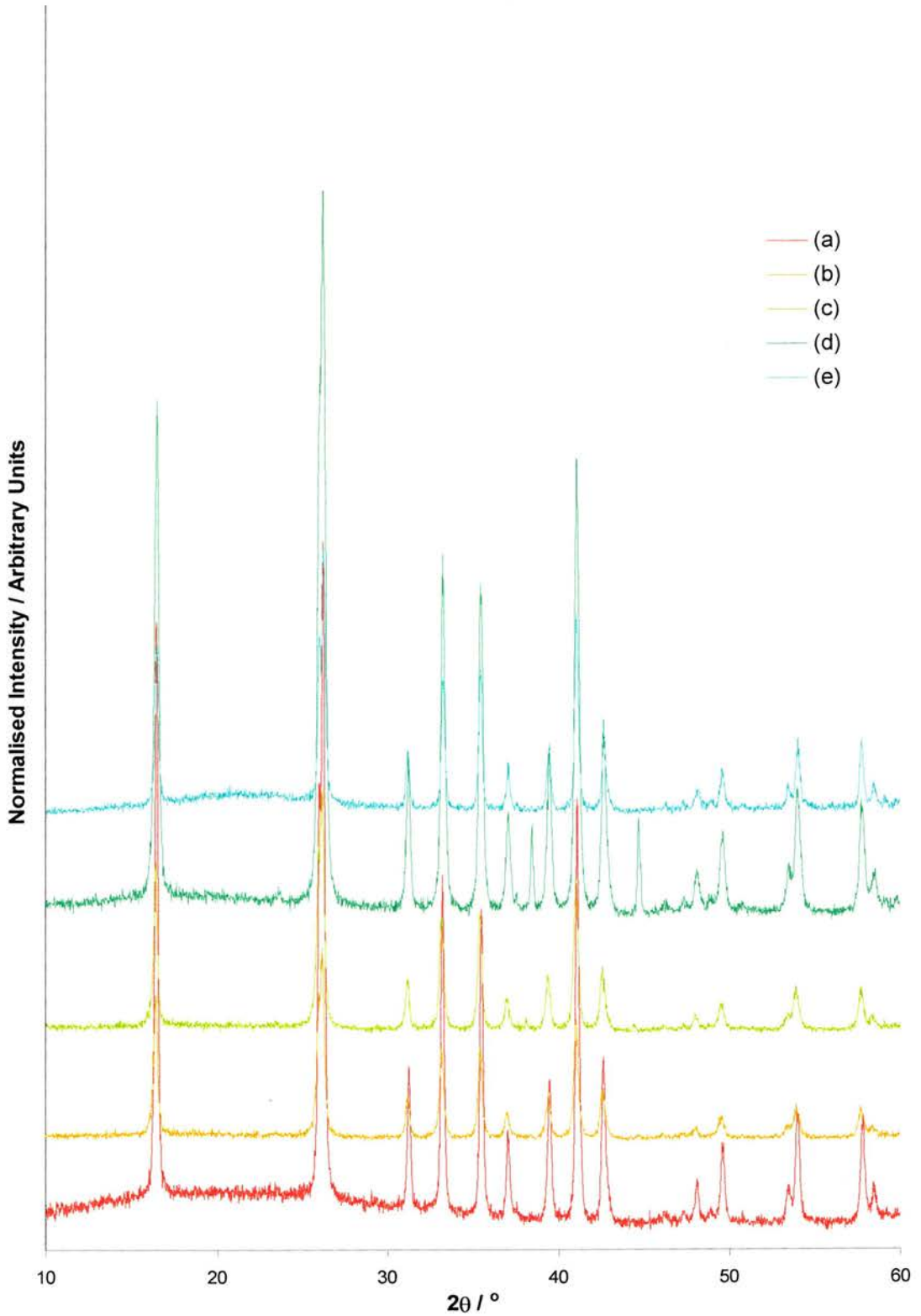


**Figure 4.13.** X-ray diffraction patterns collected from a sample of initial composition:  $1.875\text{Al}_2\text{O}_3 \cdot \text{SiO}_2 \cdot 0.125\text{B}_2\text{O}_3$  crystallised in 12 hours at (a) 1000 °C (b) 1050 °C (c) 1100 °C (d) 1150 °C (e) 1200 °C.

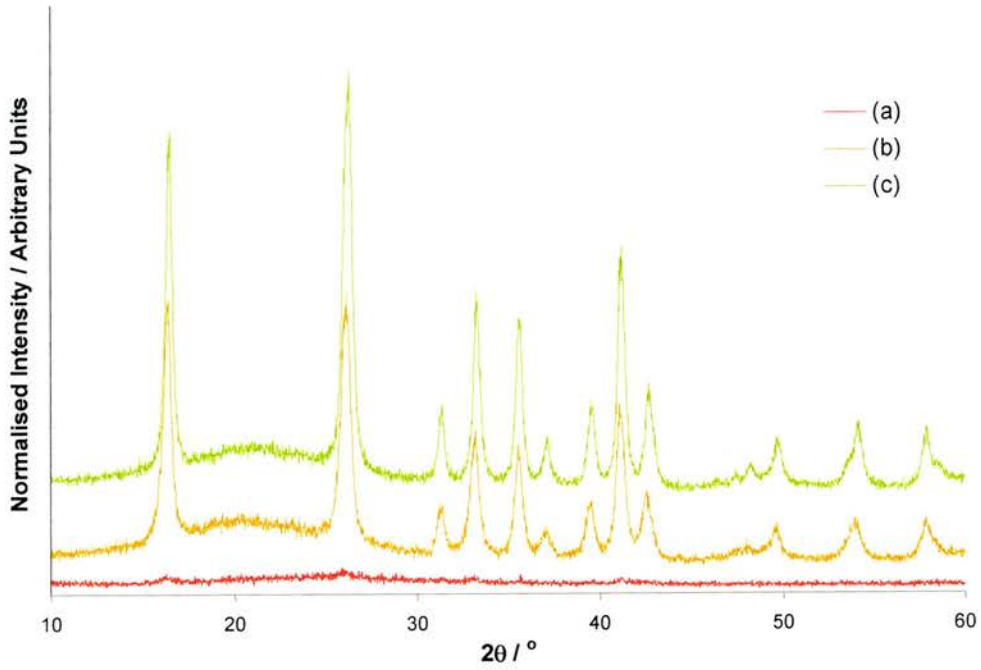


**Figure 4.14.** X-ray diffraction patterns collected from a sample of initial composition:  $6.5\text{Al}_2\text{O}_3 \cdot 5\text{SiO}_2 \cdot \text{B}_2\text{O}_3$  crystallised in 12 hours at (a) 700 °C (b) 1000 °C (c) 1200 °C.

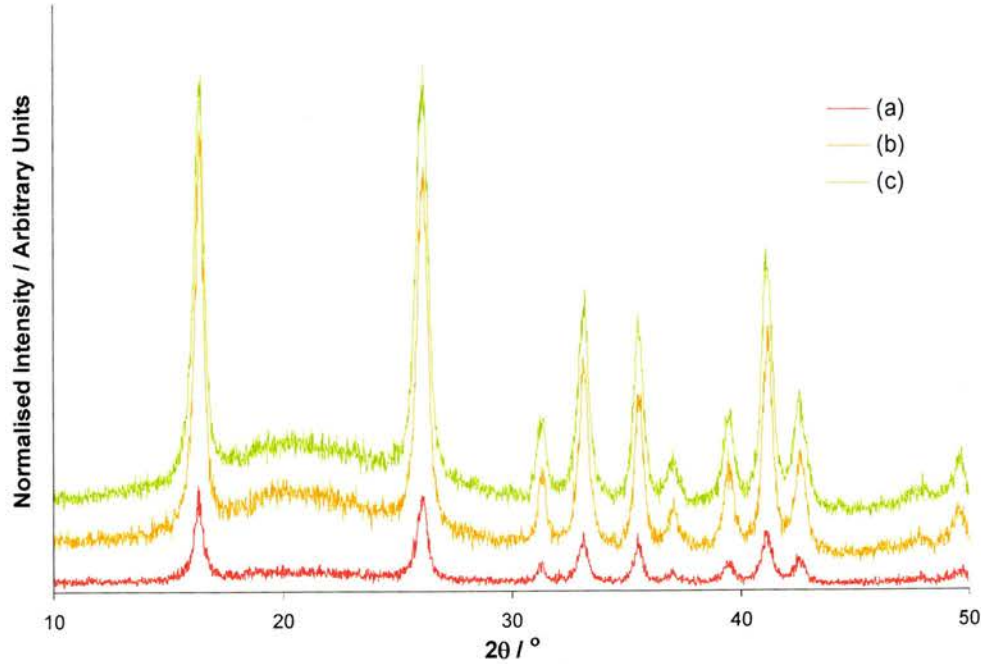


**Figure 4.15.** X-ray diffraction patterns collected from a sample of initial composition:  $6.5\text{Al}_2\text{O}_3 \cdot 5\text{SiO}_2 \cdot \text{B}_2\text{O}_3$  crystallised at 1000 °C in (a) 2.75 hours (b) 6 hours (c) 12 hours.

#### 4.4.2.2. Rietveld Refinement

The most crystalline profiles were then matched using the Rietveld method to confirm phase purity. Using the structural model proposed by Angel *et al.* and refining the instrumental parameters using the GSAS suite of programs, the close agreement of the experimental profile (crosses) and the simulated pattern (blue line), as indicated by the difference plot, shows the model to be satisfactory ( $R_{wp} = 6.61\%$ ,  $R_p = 5.18\%$ ). Unit cell parameters of  $a = 7.55521(26) \text{ \AA}$ ,  $b = 7.67852(25) \text{ \AA}$ ,  $c = 2.86627(8) \text{ \AA}$  were obtained.

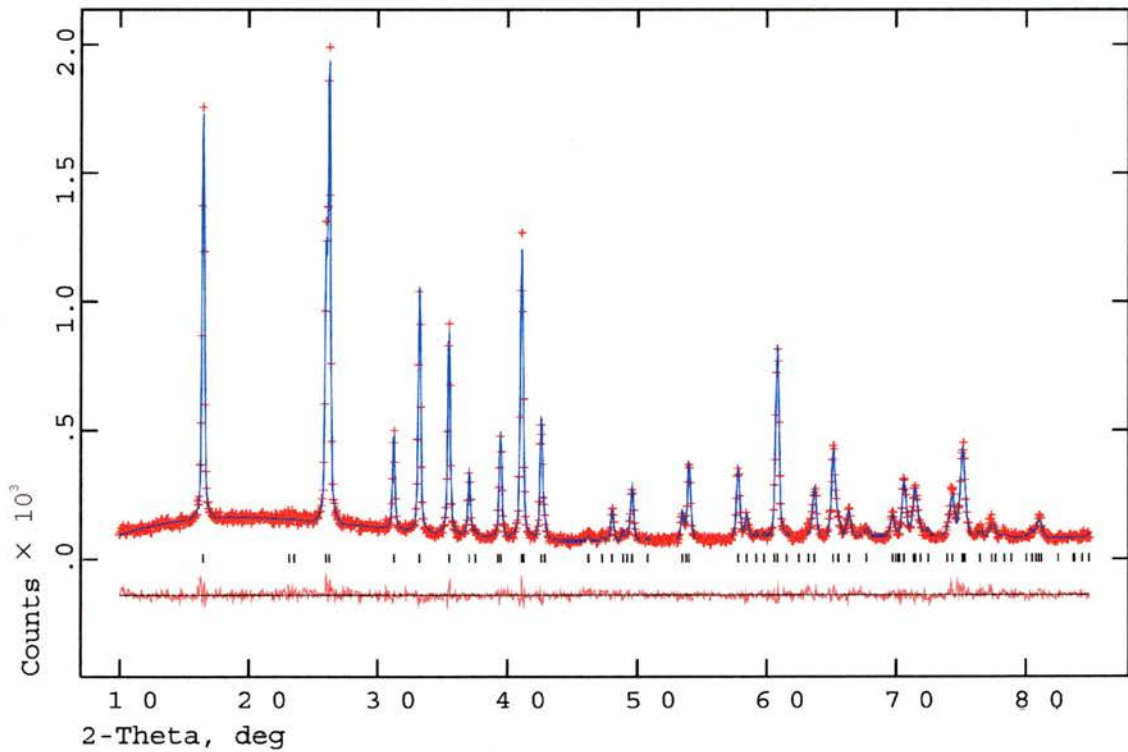


**Figure 4.16.** Rietveld refinement plot of mullite composition  $7.5\text{Al}_2\text{O}_3 \cdot 4\text{SiO}_2 \cdot 0.5\text{B}_2\text{O}_3$  showing simulated pattern (blue line), experimental profile (red crosses) and difference plot (red line).

#### 4.4.2.3. NMR Results

The boron, aluminium and silicon MAS NMR spectra of well crystalline mullite samples of composition  $1.875\text{Al}_2\text{O}_3\cdot\text{SiO}_2\cdot 0.125\text{B}_2\text{O}_3$  (formed at 1000 °C and 1200 °C) and  $8\text{Al}_2\text{O}_3\cdot 3\text{SiO}_2\cdot 0.5\text{B}_2\text{O}_3$  (formed at 1000 °C and 1200 °C) are shown in Figure 4.17. Both of these materials are representative of mullite, found within the range of compositions previously reported. In addition, a sample of composition  $6\text{Al}_2\text{O}_3\cdot 5\text{SiO}_2\cdot 1.5\text{B}_2\text{O}_3$  (formed at 1000 °C and 1200 °C), found close to the dumortierite region in the triangular composition diagram was examined (Figure 4.18). This material is richer in silica.

All six aluminium spectra show one octahedral and two tetrahedrally co-ordinated sites as previously observed in aluminosilicate mullites.  $^{27}\text{Al}$  MQ MAS NMR of the  $6\text{Al}_2\text{O}_3\cdot 5\text{SiO}_2\cdot 1.5\text{B}_2\text{O}_3$  confirms this, resolving the two tetrahedral sites (Figure 4.19).

Two distinct types of  $^{29}\text{Si}$  spectra are seen for the samples. Spectra of samples with initial compositions  $1.875\text{Al}_2\text{O}_3\cdot\text{SiO}_2\cdot 0.125\text{B}_2\text{O}_3$  and  $8\text{Al}_2\text{O}_3\cdot 3\text{SiO}_2\cdot 0.5\text{B}_2\text{O}_3$ , i.e. within the region previously observed to give mullites, show a single resonance at *ca.* -88 ppm, whereas the material of composition  $6\text{Al}_2\text{O}_3\cdot 5\text{SiO}_2\cdot 1.5\text{B}_2\text{O}_3$ , which is outside this region, gives two resonances, one at *ca.* -88 ppm and the other at *ca.* -110 ppm. Using currently accepted chemical shift scales (see for example reference 28), the resonance at -88 ppm may be assigned to  $\text{Si}-(\text{OAl})_4$  and that at -110 ppm to  $\text{Si}-(\text{OSi})_4$  groups, respectively. Whilst the former environment is expected in the mullite structure, the second is not, and suggests that a second phase, invisible to the XRD, is present.

Similarly,  $^{11}\text{B}$  NMR differs between the two sets of samples described above. Those within the pre-described mullite region are explained by a trigonal species with axial symmetry and a small, but variable, amount (1 – 2 %) of four-co-ordinate boron; whereas the sample outside this region possesses a more complex spectrum, particularly at the higher temperature. (Simulation of the  $^{11}\text{B}$  peak shape of the material crystallised at 1200 °C with composition  $8\text{Al}_2\text{O}_3\cdot 3\text{SiO}_2\cdot 0.5\text{B}_2\text{O}_3$  yielded a coupling constant of 2.57 MHz, asymmetry of 0.16 and an isotropic shift of 16.8 when 2 % four-co-ordinate boron was assumed.)

To further investigate the environments of boron in the  $6\text{Al}_2\text{O}_3 \cdot 5\text{SiO}_2 \cdot 1.5\text{B}_2\text{O}_3$  sample a MQ MAS NMR spectrum was run. This permitted the identification of two distinct trigonal sites, at *ca.* 82 and 104 ppm on the F1 axis, and a tetrahedral site, at *ca.* 2 ppm on the F1 axis (Figure 4.20.).

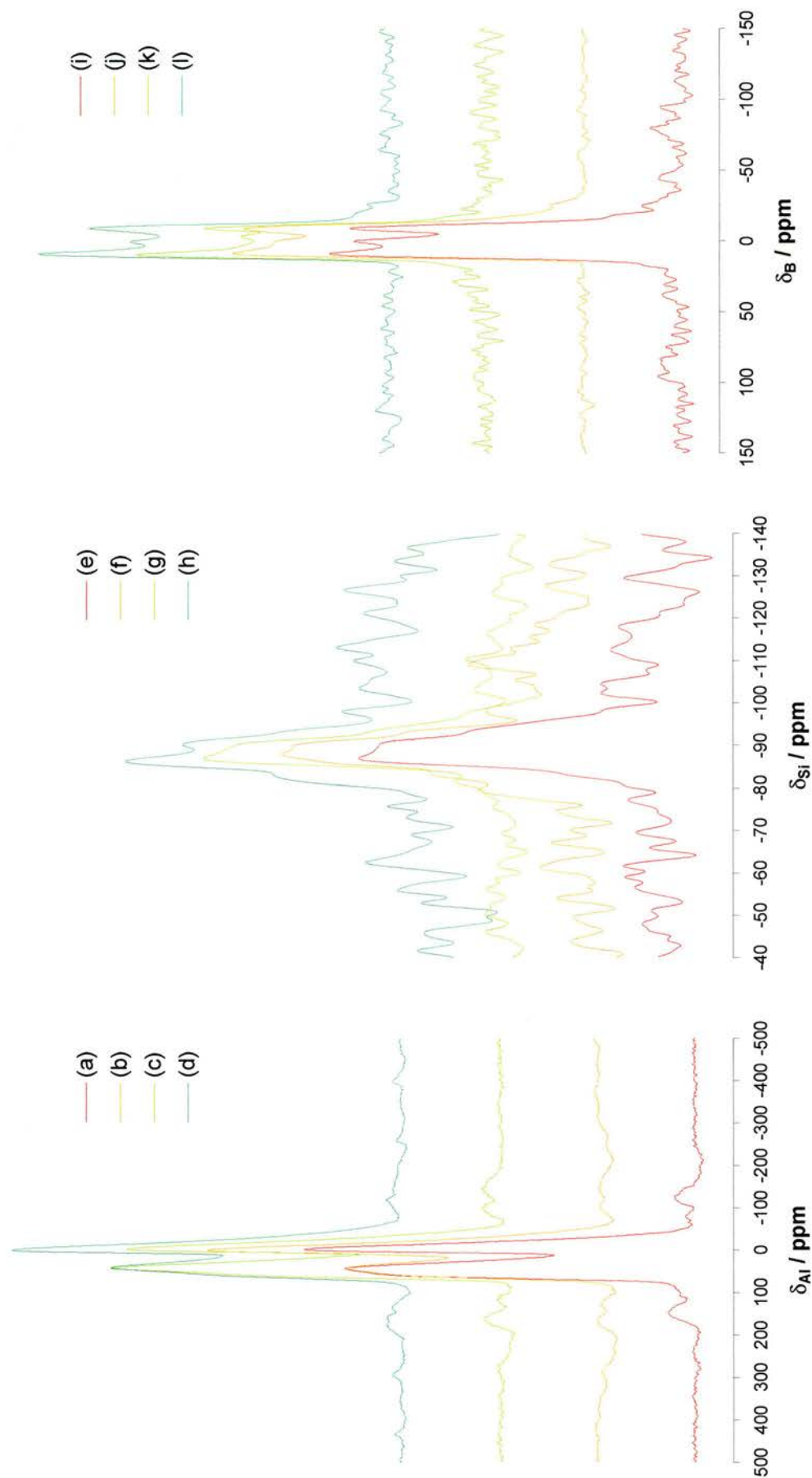


**Figure 4.17.**  $1.875\text{Al}_2\text{O}_3 \cdot \text{SiO}_2 \cdot 0.125\text{B}_2\text{O}_3$  crystallised at  $1000^\circ\text{C}$ : (a)  $^{27}\text{Al}$  MAS NMR, (e)  $^{29}\text{Si}$  MAS NMR, (i)  $^{11}\text{B}$  MAS NMR; and  $1200^\circ\text{C}$ : (c)  $^{27}\text{Al}$  MAS NMR, (g)  $^{29}\text{Si}$  MAS NMR, (k)  $^{11}\text{B}$  MAS NMR;  $8\text{Al}_2\text{O}_3 \cdot 3\text{SiO}_2 \cdot 0.5\text{B}_2\text{O}_3$  crystallised at  $1000^\circ\text{C}$ : (b)  $^{27}\text{Al}$  MAS NMR, (f)  $^{29}\text{Si}$  MAS NMR, (j)  $^{11}\text{B}$  MAS NMR; and  $1200^\circ\text{C}$ : (d)  $^{27}\text{Al}$  MAS NMR, (h)  $^{29}\text{Si}$  MAS NMR, (l)  $^{11}\text{B}$  MAS NMR.

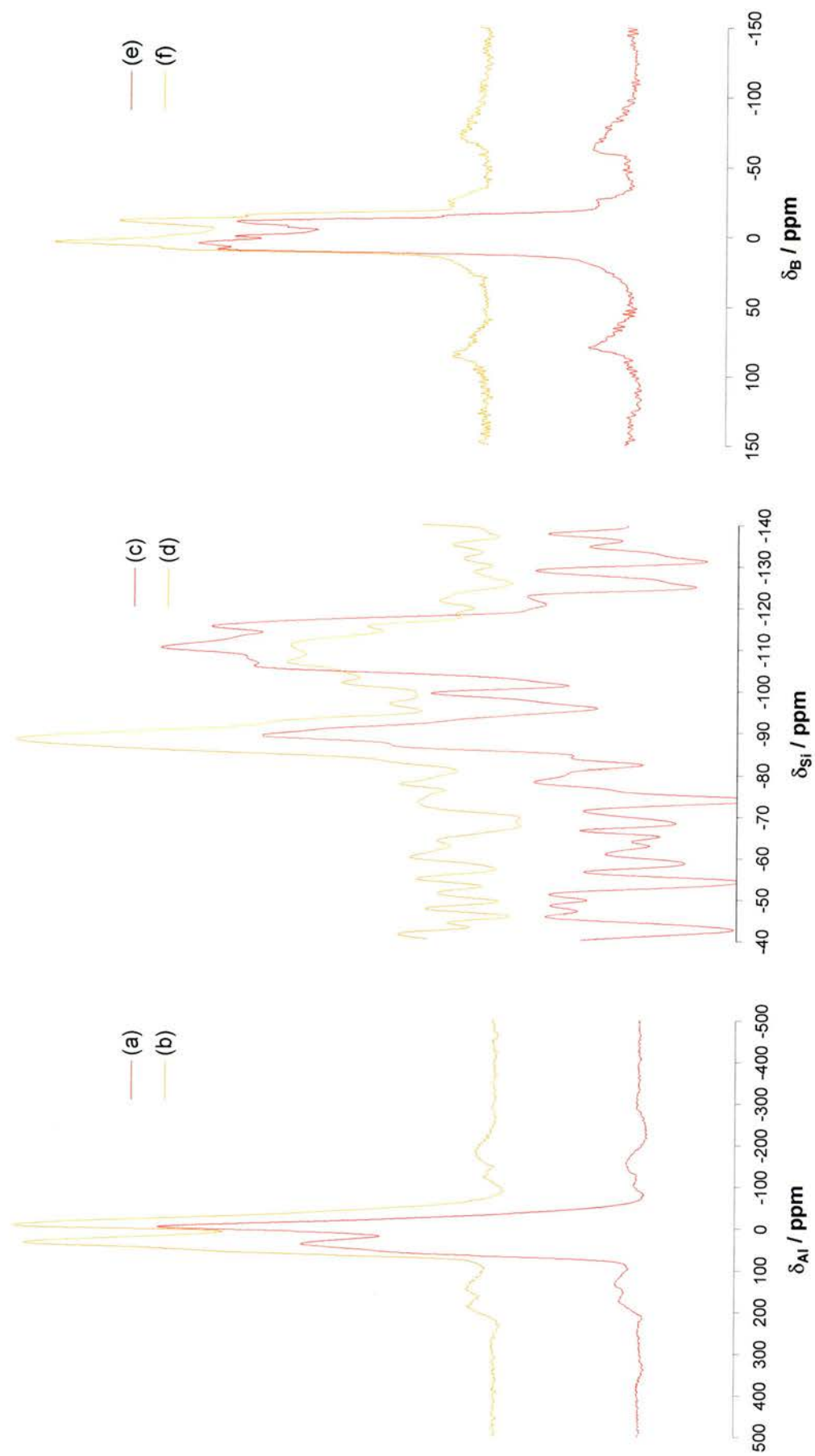


**Figure 4.18.**  $6\text{Al}_2\text{O}_3 \cdot 5\text{SiO}_2 \cdot 1.5\text{B}_2\text{O}_3$  crystallised at  $1000^\circ\text{C}$ : (a)  $^{27}\text{Al}$  MAS NMR, (c)  $^{29}\text{Si}$  MAS NMR, (e)  $^{11}\text{B}$  MAS NMR; and at  $1200^\circ\text{C}$ : (b)  $^{27}\text{Al}$  MAS NMR, (d)  $^{29}\text{Si}$  MAS NMR, (f)  $^{11}\text{B}$  MAS NMR.

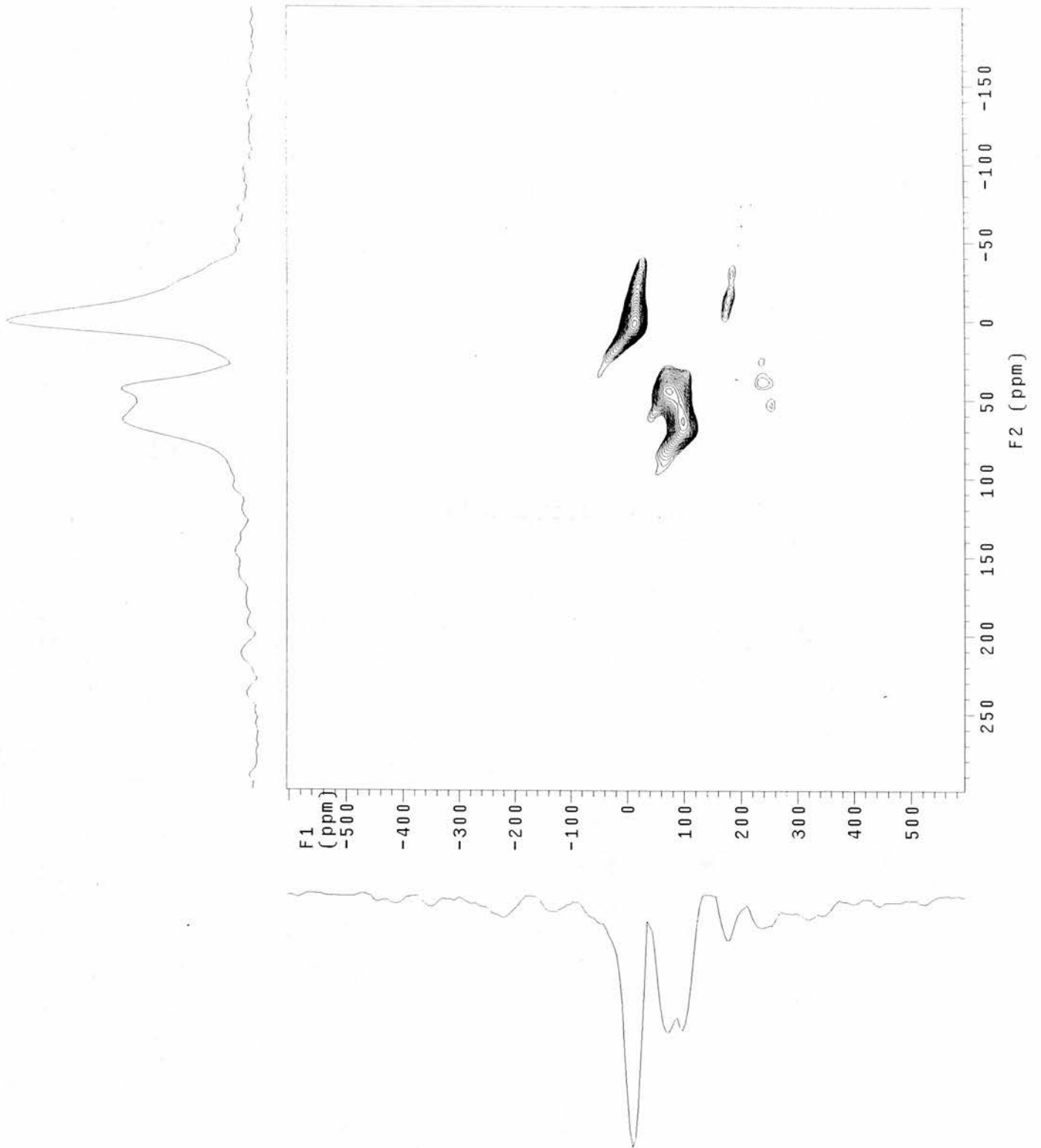
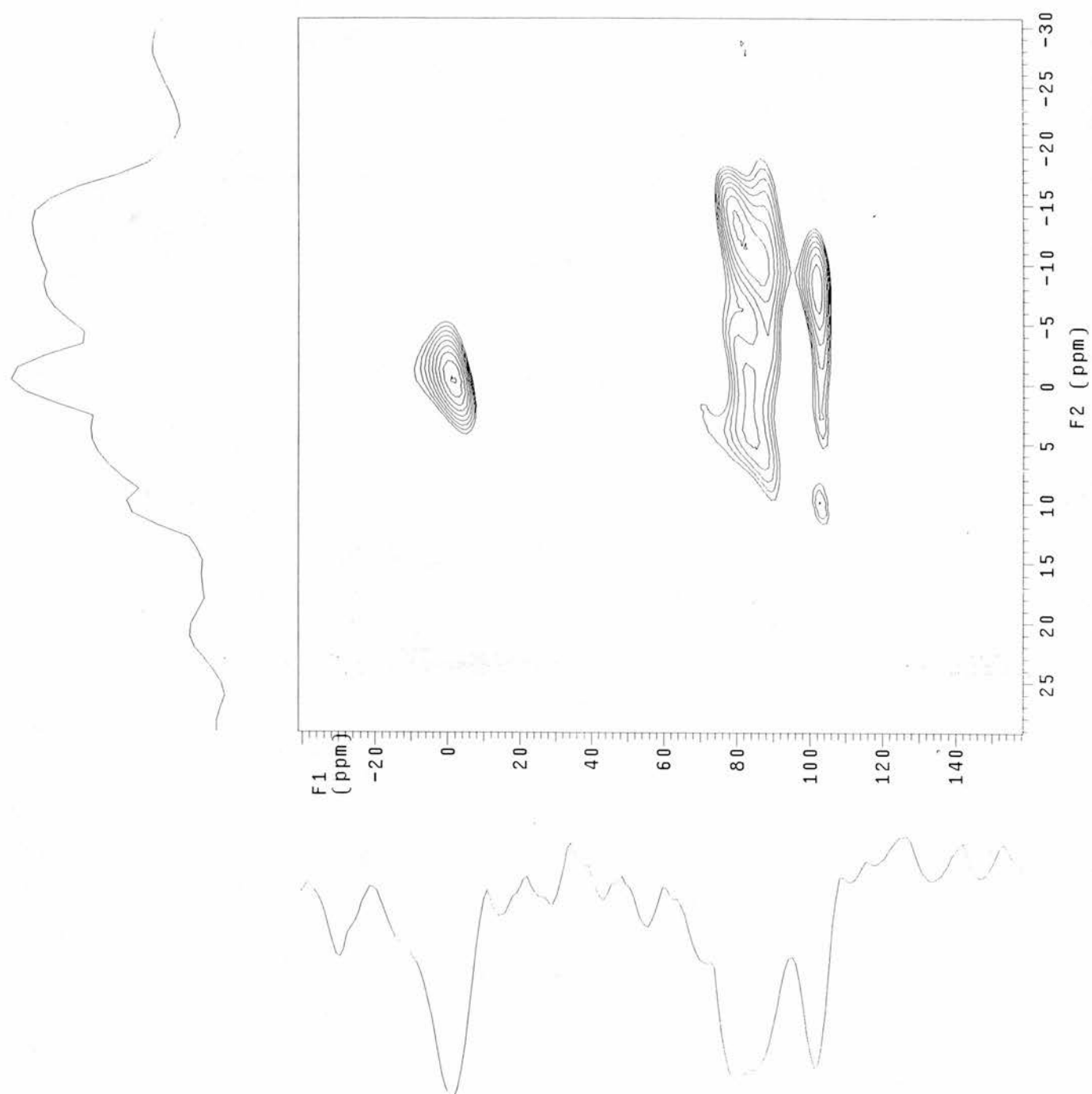


Figure 4.19.  $^{27}\text{Al}$  MQ MAS NMR spectrum showing two tetrahedral sites.



**Figure 4.20.**  $^{11}\text{B}$  MQ MAS NMR spectrum showing two distinct trigonal sites and one tetrahedral site.

## 4.5. Discussion

It has been demonstrated that the sol-gel method for preparing mullite and related ceramic materials works well, particularly in the presence of boron. Phase pure mullites are obtained with reasonable crystallinity at temperatures of 900 °C and above. This compares favourably with solid state synthetic procedures.<sup>22</sup>

Examination of aluminoborates (without silicon) confirmed previous reports that mullite-like phases can be prepared, and that at temperatures above 1000 °C these break-down to give the known  $9\text{Al}_2\text{O}_3 \cdot 2\text{B}_2\text{O}_3$  phase (plus any excess alumina). Comparison of starting compositions with final X-ray diffraction patterns for the 1 : 1 phase indicates loss of boron over 24 hours at 1100 °C. During the evolution of the mullite, broad peaks are observed in the X-ray diffraction pattern that suggest domains of ordering in the sample. ( $a = 7.498\text{Å}$ ,  $b = 7.683\text{Å}$ ,  $c = 2.830\text{Å}$  for aluminoborate mullite,  $a = 7.677\text{Å}$ ,  $b = 14.983\text{Å}$ ,  $c = 5.656\text{Å}$  for  $9\text{Al}_2\text{O}_3 \cdot 2\text{B}_2\text{O}_3$ ).  $^{11}\text{B}$  NMR indicates, for the first time, that boron in the precursor mullite is in trigonal co-ordination, rather than tetrahedral. This suggests that it can exist within the mullite structure in a very similar environment to that it occupies in the crystalline  $9\text{Al}_2\text{O}_3 \cdot 2\text{B}_2\text{O}_3$  phase (see Figure 4.6. for comparison).

For boro-aluminosilicates,  $^{29}\text{Si}$  and  $^{11}\text{B}$  NMR may be used to establish phase purity more conclusively than  $^{27}\text{Al}$  NMR or X-ray diffraction. For boro-aluminosilicate mullites, it is also observed by NMR that the phase is truly phase pure. Boron exists largely in trigonal co-ordination in the mullite, and again is similar to that found in the  $9\text{Al}_2\text{O}_3 \cdot 2\text{B}_2\text{O}_3$  phase.

## 4.6 Conclusions

Boron was found to accelerate mullite crystallisation but is partially lost at higher temperatures. Aluminoborate mullite was observed which broke down at higher temperatures to the phase  $9\text{Al}_2\text{O}_3 \cdot 2\text{B}_2\text{O}_3$  and alumina. Boro-mullite that was phase pure by XRD was seen to crystallise over a wider range of compositions than previously reported but  $^{29}\text{Si}$  and  $^{11}\text{B}$  NMR spectroscopy indicates the presence of other phases outside the field reported to give mullite previously. Assuming the boron is present in the mullite structure, it is hypothesised that it is in a related

trigonal site to that observed in  $9\text{Al}_2\text{O}_3 \cdot 2\text{B}_2\text{O}_3$ , rather than in a tetrahedral site as was proposed before.

#### 4.7. Further Work

EELS (electron energy loss spectroscopy) studies<sup>24</sup> are in progress to establish semi-quantitatively the boron contents of these samples, and to confirm whether the boron is in the crystalline phases or external to them. (EELS is known to be very sensitive to the analysis of light elements.)

The thermal expansion properties of all the  $\text{Al}_2\text{SiO}_5$  polymorphs were investigated by Winter and Ghose,<sup>25</sup> who showed that the macroscopic changes in unit cell parameters could be rationalised with reference to the Al–O<sub>d</sub> bond length and orientation. For example, the shorter and stronger bond in sillimanite expanded less than in the analogous bond in andalusite. Schneider *et al.*<sup>26</sup> studied aluminosilicate mullite and found discontinuous expansion along the crystallographic *a*, *b* and *c*-axes that was low and non-linear between 25 and 200 °C, linear between 200 and 400 °C but discontinuous between 400 and 500 °C while linear again between 500 and 800 °C. No mechanism was proposed to account for the discontinuity. On the basis of the Winter *et al.* mechanism Garsche *et al.*<sup>27</sup> proposed that  $9\text{Al}_2\text{O}_3 \cdot 2\text{B}_2\text{O}_3$  would show low thermal expansion. It would be interesting to measure such values for this and boro-aluminosilicate materials.

#### 4.8 References

1. E. Zen, *Amer. J. Sci.*, 1969, **267**, 297.
2. W. E. Cameron and J. R. Ashworth, *Nature (London)*, 1972, **235**, 134.
3. K. Sahl and F. Seifert, *Nature (London)*, 1973, **241**, 46.
4. D. Kerrick, in *Reviews in Mineralogy*, ed. P. H. Ribbe, Mineralogical Society of America, Washington DC, 1st edn., 1990, vol. 22, ch. 6, pp. 201–205.
5. C. W. Burnham, *Compositional Limits of Mullite, and the Sillimanite–Mullite Solid Solution Problem*, Ann. Rept Dir. Geophys. Lab. 1963–64, Carnegie Inst., Washington, 1964.
6. W. Guse, H. Saalfeld and J. Tjandra, *N. Jahrb. Mineral. Monatsh.*, 1979, **4**, 175.
7. R. X. Fischer, H. Schneider and M. Schmücker, *Am. Mineral.*, 1994, **79**, 983.

8. W. E. Cameron, *Am. Mineral.*, 1977, **62**, 747.
9. T. Ban and K. Okada, *J. Am. Ceram. Soc.*, 1992, **75**, 227.
10. F. J. Klug, S. Prochazka and R. H. Doremus, *Ceram. Trans.*, 1990, **6**, 15.
11. W. E. Cameron, *Ceram. Bul.*, 1977, **56**, 1003.
12. H. Schneider, R. X. Fischer and D. Voll, *J. Am. Ceram. Soc.*, 1993, **76**, 1879.
13. R. J. Angel and T. Prewitt, *Am. Mineral.*, 1986, **71**, 1476.
14. R. Sadanaga, M. Tokonami and Y. Takéuchi, *Acta Cryst.*, 1962, **15**, 65
15. S. Durovic, *Chem. Zvesti*, 1969, **23**, 113.
16. C. W. Burnham, *The Crystal Structure of Mullite*, Ann. Rept Dir. Geophys. Lab. 1962–63, Carnegie Inst., Washington, 1963.
17. P. Rehak, G. Kunath-Fandrei, P. Losso, B. Hildmann, H. Schneider and C. Jäger, *Am. Mineral.*, 1998, **83**, 1266.
18. E. S. Grew and L. M. Anovitz, *Reviews in Mineralogy*, ed. P. H. Ribbe, Mineralogical Society of America, Washington DC, 1st edn., 1996, vol. 33, ch. 3 p. 127
19. D. Mazza, M. Vallino and G. Busco, *J. Am. Ceram. Soc.*, 1992, **75**, 1929.
20. A. Dietzel and H. Scholze, *Glastechn. Ber.*, 1955, 47.
21. M. Ihara, K. Imai, J. Fukunaga and N. Yoshida, *Yogyo Kyokaishi*, 1980, **88**, 77.
22. A. Taylor and D. Holland, *J. Non-Cryst. Solids*, 1993, **152**, 1.
23. A. C. Larson and R. B. Von Dreele, Los Alamos National Laboratory Report No. LA-UR-86-748, 1987.
24. L. A. J. Garvie and P. R. Buseck, in *Reviews in Mineralogy*, ed. P. H. Ribbe, Mineralogical Society of America, Washington DC, 1st edn., 1996, vol. 33, ch. 18, pp. 821–843.
25. J. K. Winter and S. Ghose, *Am. Mineral.*, 1979, **64**, 573.
26. H. Schneider, K. Rodewald and E. Eberhard, *J. Am. Ceram. Soc.*, 1993, **76**, 2896.
27. M. Garsche, E. Tillmanns, H. Almen, H. Schneider and V. Kupcik, *Eur. J. Mineral.*, 1991, **3**, 793.
28. C. A. Fyfe and R. E. Wasylshen, in *Solid State Chemistry: Techniques*, eds. A. K. Cheetham and P. Day, Oxford University Press, Oxford, 1987, ch. 6, pp. 190–230.